J. Fluid Mech. (1995), *vol.* 293, *pp.* 47–80

Rotating free-shear flows. Part 2. Numerical simulations

By OLIVIER MÉTAIS[1], CARLOS FLORES[2], SHINICHIRO YANASE[3], JAMES J. RILEY[4] AND MARCEL LESIEUR[1]

[1]Laboratoire des Écoulements Géophysiques et Industriels de Grenoble, URA CNRS 1509,
Institut de Mécanique de Grenoble, Institut National Polytechnique et Université Joseph Fourier,
Grenoble, BP 53, 38041 Grenoble Cédex 9, France

[2]Departemento de Oceanografia- CFE, Mexico, DF, 03810, Mexico

[3]Engineering Mathematics, Faculty of Engineering, Okayama University, Tsushimanaka,
Okayama 700, Japan

[4]Department of Mechanical Engineering, University of Washington, Seattle, WA 98195, USA

(Received 23 June 1994 and in revised form 9 February 1995)

The three-dimensional dynamics of the coherent vortices in periodic planar mixing layers and in wakes subjected to solid-body rotation of axis parallel to the basic vorticity are investigated through direct (DNS) and large-eddy simulations (LES). Initially, the flow is forced by a weak random perturbation superposed on the basic shear, the perturbation being either quasi-two-dimensional (forced transition) or three-dimensional (natural transition). For an initial Rossby number $R_o^{(i)}$, based on the vorticity at the inflexion point, of small modulus, the effect of rotation is to always make the flow more two-dimensional, whatever the sense of rotation (cyclonic or anticyclonic). This is in agreement with the Taylor–Proudman theorem. In this case, the longitudinal vortices found in forced transition without rotation are suppressed.

It is shown that, in a cyclonic mixing layer, rotation inhibits the growth of three-dimensional perturbations, whatever the value of the Rossby number. This inhibition exists also in the anticyclonic case for $|R_o^{(i)}| \leqslant 1$. At moderate anticyclonic rotation rates ($R_o^{(i)} < -1$), the flow is strongly destabilized. Maximum destabilization is achieved for $|R_o^{(i)}| \approx 2.5$, in good agreement with the linear-stability analysis performed by Yanase *et al.* (1993). The layer is then composed of strong longitudinal alternate absolute vortex tubes which are stretched by the flow and slightly inclined with respect to the streamwise direction. The vorticity thus generated is larger than in the nonrotating case. The Kelvin–Helmholtz vortices have been suppressed. The background velocity profile exhibits a long range of nearly constant shear whose vorticity exactly compensates the solid-body rotation vorticity. This is in agreement with the phenomenological theory proposed by Lesieur, Yanase & Métais (1991). As expected, the stretching is more efficient in the LES than in the DNS.

A rotating wake has one side cyclonic and the other anticyclonic. For $|R_o^{(i)}| \leqslant 1$, the effect of rotation is to make the wake more two-dimensional. At moderate rotation rates ($|R_o^{(i)}| > 1$), the cyclonic side is composed of Kármán vortices without longitudinal hairpin vortices. Kármán vortices have disappeared from the anticyclonic side, which behaves like the mixing layer, with intense longitudinal absolute hairpin vortices. Thus, a moderate rotation has produced a dramatic symmetry breaking in the wake topology. Maximum destabilization is still observed for $|R_o^{(i)}| \approx 2.5$, as in the linear theory.

The paper also analyses the effect of rotation on the energy transfers between the mean flow and the two-dimensional and three-dimensional components of the field.

1. Introduction

Turbulent or transitional shear flows in a rotating frame have been extensively studied owing to their importance in many geophysical and engineering applications. Within these flows, the local Rossby number, which characterizes the relative importance of inertial and Coriolis forces, can vary significantly. Typical values of the Rossby number are on the order of 0.05 in mesoscale oceanic eddies and in Jupiter's Great Red Spot, 0.3 for large synoptic-scale atmospheric perturbations, and 2.5 for the atmospheric wake of a small island. Turbulence in rotating fluids finds numerous industrial applications in turbo-machinery; e.g. the turbulent characteristics of the flow in blade passages of radial pumps and compressor impellers determine the efficiency of these devices. Turbulence is also of great importance for the cooling by the fluid inside the blades. Depending upon the magnitude of the radial velocity, the Rossby number within rotating machines can range from values close to unity to very small ones (of the order 0.05).

Owing to their engineering applications, early experiments have focused on rotating bounded flows such as boundary layers over flat surfaces and flow in a straight channel. Several basic features of the boundary layers over rotating solid surfaces have been determined (see e.g. Hart 1971 for the laminar channel flow; Johnston, Haleen & Lesius 1972 for the turbulent channel flow; Potter & Chawla 1971 for the laminar boundary layer; Watmuff, Witt & Joubert 1985 for the turbulent boundary layer). Let $\bar{\boldsymbol{u}} = (\bar{u}, 0, 0)$ be the mean velocity (x is in the streamwise direction and y in the direction perpendicular to the wall). The rotation vector $\boldsymbol{\Omega} = (0, 0, \Omega)$ is oriented along the spanwise direction z, and may be positive or negative. For the channel flow, the vorticity vector associated with the mean velocity profile $\omega = (0, 0, -\mathrm{d}\bar{u}/\mathrm{d}y)$ is parallel to $\boldsymbol{\Omega}$ near one wall and antiparallel near the opposite wall; we refer to flow near these two particular walls as cyclonic and anticyclonic, respectively. Various other terms are currently used. The names suction and pressure sides originate from the pressure gradient due to the Coriolis force, and the terms trailing and leading sides are borrowed from the turbo-machinery literature. The laboratory experiments have shown that the cyclonic side is stabilized; as compared to the non-rotating case, the turbulence energy production decreases with increasing rotation rate and fast rotation can lead to the total suppression of turbulent transition. Conversely, the anticyclonic side is destabilized for moderate rotation rates (high enough Rossby numbers), and develops an instability in the form of large periodic longitudinal rolls. Numerical simulations of rotating channel flows (Kim 1983; Tafti & Vanka 1991; Guo & Finlay 1991; Kristoffersen & Andersson 1993) have complemented the experimental investigations by studying in detail the influence of the rotation on the three-dimensional coherent structures. No experimental or numerical data seem to be available for high rotation rates in the anticyclonic case.

For free-shear flows, the drastically different effects of solid-body rotation, depending on whether the sense of rotation is cyclonic or anticyclonic, have been investigated in several laboratory experiments. Rothe & Johnston (1979) have analysed the large-eddy spanwise structures (Kelvin–Helmholtz vortices) present in the reattaching shear layer generated by the flow over a backward-facing step. The channel in which the step is placed rotates about the spanwise axis. The reattachment length in both cyclonic and anticyclonic regimes is found to be notably different. In the cyclonic case, it is longer than in the absence of rotation: cyclonic rotation suppresses the three-dimensional turbulence and reinforces the spanwise vortices shed behind the step. When the test section was rotated in the opposite direction, the strength of the three-dimensional instabilities was enhanced and the reattachment length was shortened. The rotating mixing layer experiment (rotation axis oriented along the span) by Bidokhti & Tritton (1992) has confirmed the fact that the cyclonic eddies are rendered more two-dimensional. Conversely, Kelvin–Helmholtz vortices seem to be completely disrupted, even by a weak anticyclonic rotation. Furthermore, the measurement of Reynolds stresses indicates that this destabilization occurs in the early stage of the mixing layer development and is followed by a subsequent two-dimensionalization. Destabilization of Kelvin–Helmholtz vortices and subsequent two-dimensionalization can be simultaneously observed in flows like rotating wakes or jets. Witt & Joubert (1985) found that the wake of a cylinder whose axis is parallel to $\boldsymbol{\Omega}$ exhibits asymmetry for the mean flow as well as for the turbulent quantities. This is confirmed by Chabert d'Hières, Davies & Didelle (1988); they show that, at moderate rotation rates, the cyclonic vortices of the wake are reinforced while the anticyclonic ones are destroyed. Conversely, the wake is reorganized into a very regular two-dimensional Kármán street of alternate vortices at high rotation rates. Satellite observations of atmospheric wakes displayed by clouds also exhibit strong asymmetrical eddy structures (Etling 1990).

Therefore, there are three basic effects associated with rotating bounded- or free-shear flows. (i) If the shear vorticity is parallel to and of same sign as the rotation vector, the flow is made more two-dimensional. (ii) If the two vectors are anti-parallel, destabilization is observed at moderate rotation rates, while (iii) two-dimensionalization is recovered for fast rotation. For a two-dimensional flow in a plane perpendicular to the rotation axis, the Coriolis force is proportional to the gradient of the stream function, and may be included with the pressure. Therefore, without change of the boundary conditions relative to the rotating axes, a solid-body rotation of a two-dimensional flow system does not modify the velocity distribution. Thus, the phenomena observed in the laboratory experiments can only be explained by considering the influence of rotation on the growth of three-dimensional perturbations.

1.1. *Linear-stability analysis*

In order to describe the early stage of the development, Yanase *et al.* (1993) have performed a three-dimensional, viscous, linear-stability analysis of two planar free-shear flows subject to rigid-body rotation oriented along the span: the mixing layer and the plane wake. The mean velocity is oriented in the longitudinal direction x and varies with y, $[\bar{u}(y), 0, 0]$. The rotation vector is the spanwise direction z, $\boldsymbol{\Omega} = (0, 0, \Omega)$. The Rossby number is here based upon the maximum vorticity of the basic profile, that is, the vorticity at the inflexion point(s), $-(\mathrm{d}\bar{u}/\mathrm{d}y)_i$, i.e.

$$R_o = -(\mathrm{d}\bar{u}/\mathrm{d}y)_i/2\Omega \quad . \tag{1.1}$$

In the mixing layer, R_o is positive for cyclonic rotation and negative for anticyclonic rotation. For the wake, one considers the modulus $|R_o|$ of the Rossby number. From the linearized governing equations, it is shown that cyclonic rotation prevents the growth of three-dimensional perturbations and two-dimensionalization is observed. For strong anticyclonic rotation ($R_o > -1$) the effect is similar. For moderate anticyclonic rotation ($R_o < -1$), however, the flow stability is dramatically modified. In this regime, a new instability appears along the k_z-axis ($k_x = 0$), corresponding to a purely streamwise instability. Following Bidokhti & Tritton (1992), this will be designated the shear/Coriolis instability. For both the mixing layer and the wake, this shear/Coriolis instability has larger amplification rates than the co-existing Kelvin–Helmholtz instability for roughly the range $-8 < R_o < -1.5$, and its effect is maximum for $R_o \approx -2.5$. Yanase *et al.* (1993) have also shown that, for purely longitudinal modes ($k_x = 0$), and if the stability problem is reduced to perturbations such that $k_x = 0$, a necessary and sufficient condition for inviscid instability is that the local Rossby number $R_o(y) = -(\mathrm{d}\bar{u}/\mathrm{d}y)/2\Omega$ should be smaller than -1 somewhere in the layer. This result was previously found by Pedley (1969) and Hart (1971). A similar criterion, based upon an analogy with stratified flows, was proposed by Bradshaw (1969) and later reproduced by Tritton & Davies (1985) through phenomenological arguments.

For a purely longitudinal perturbation, the eigenvalue equation is similar to the one governing the radial velocity when studying the inviscid linear centrifugal instability in the limit of axisymmetric disturbances. This emphasizes the close relationship between the present problem and the stability of flows between rotating, concentric cylinders (the Couette–Taylor problem), flows in curved channels (the Dean problem), and flows along curved boundaries (the Görtler problem). In each of these cases, the instability leads to the amplification of a purely streamwise mode, which eventually produces vortices aligned with the basic velocity streamlines: Couette–Taylor vortices, Görtler vortices, etc.

1.2. *Vorticity dynamics*

1.2.1. *Quasi-linear theory*

Further insight into the shear/Coriolis instability can be obtained by examining the vorticity dynamics. We considerer a Cartesian reference frame $\boldsymbol{x} = (x, y, z)$ rotating with angular velocity $\boldsymbol{\Omega}$ oriented along the z-axis. Here $\boldsymbol{u} = (u, v, w)$ designates the relative velocity. Adding to the relative vorticity $\boldsymbol{\omega}$ the solid-body rotation vorticity $2\boldsymbol{\Omega}$ (entrainment vorticity), one obtains the absolute vorticity $\boldsymbol{\omega}_a = \boldsymbol{\omega} + 2\boldsymbol{\Omega}$, the vorticity of the fluid in the absolute frame. The equation for the absolute vorticity is

$$\frac{\mathrm{d}\boldsymbol{\omega}_a}{\mathrm{d}t} = (\boldsymbol{\omega}_a \cdot \nabla)\boldsymbol{u} + \nu\nabla^2\boldsymbol{\omega}_a \ , \tag{1.2}$$

where $\mathrm{d}/\mathrm{d}t$ stands for the substantial derivative. Writing the velocity and relative vorticity as sums of the basic fields plus a small perturbation, $\boldsymbol{u}'(x, y, z, t)$ and $\boldsymbol{\omega}'(x, y, z, t)$, yields:

$$\boldsymbol{u}(x, y, z, t) = \bar{u}(y)\ \boldsymbol{x} + \boldsymbol{u}'(x, y, z, t) \ , \tag{1.3}$$

$$\boldsymbol{\omega}_a(x, y, z, t) = \left(2\Omega - \frac{\mathrm{d}\bar{u}}{\mathrm{d}y}\right)\ z + \boldsymbol{\omega}'(x, y, z, t) \quad . \tag{1.4}$$

Substituting this into (1.2), one obtains to the lowest order (for a perfect fluid)

$$\frac{\bar{\mathrm{d}}\omega'_x}{\mathrm{d}t} = \omega'_y \frac{\mathrm{d}\bar{u}}{\mathrm{d}y} + \left(2\Omega - \frac{\mathrm{d}\bar{u}}{\mathrm{d}y}\right)\frac{\partial u'}{\partial z} = 2\Omega\frac{\partial u'}{\partial z} - \frac{\mathrm{d}\bar{u}}{\mathrm{d}y}\frac{\partial w'}{\partial x} \ , \tag{1.5}$$

$$\frac{\bar{\mathrm{d}}\omega'_y}{\mathrm{d}t} = \left(2\Omega - \frac{\mathrm{d}\bar{u}}{\mathrm{d}y}\right)\frac{\partial v'}{\partial z} \ , \tag{1.6}$$

where $\bar{\mathrm{d}}/\mathrm{d}t$ stands now for the substantial derivative following the basic flow, and ω'_x and ω'_y are the components of $\boldsymbol{\omega}'$ in x and y. Assuming $\partial/\partial x(\cdot) = 0$ (the shear/Coriolis instability), and under the simplifying assumption that $-\partial v'/\partial z \approx \omega'_x$, equations (1.5) and (1.6) reduce to

$$\frac{\bar{\mathrm{d}}\omega'_x}{\mathrm{d}t} = 2\Omega\omega'_y \, , \tag{1.7}$$

$$\frac{\bar{\mathrm{d}}\omega'_y}{\mathrm{d}t} = -\left(2\Omega - \frac{\mathrm{d}\bar{u}}{\mathrm{d}y}\right)\omega'_x \quad . \tag{1.8}$$

This quasi-linear model has been suggested by Tritton (1991, private communication). Equations (1.7) and (1.8) can also be recovered by considering an exact solution of Euler's equations in terms of sheets of fluid moving independently (Métais *et al.* 1992). The perturbation equations (1.7) and (1.8) then reduce to the following equation for ω'_x:

$$\frac{\mathrm{d}^2\omega'_x}{\mathrm{d}t^2} = -2\Omega\left(-\frac{\mathrm{d}\bar{u}}{\mathrm{d}y} + 2\Omega\right)\omega'_x \quad . \tag{1.9}$$

This indicates, that, in the linear regime, the longitudinal vorticity component grows exponentially in the regions such that $R_o < -1$, in agreement with the results of the linear-stability analysis. Furthermore, for a given background vorticity $-\mathrm{d}\bar{u}/\mathrm{d}y$ and varying Ω, maximum amplification is achieved for $R_o = -2$. In this case, (1.7) and (1.8) imply the same amplification rate for ω'_x and ω'_y, since

$$\frac{1}{\omega'_x}\frac{\mathrm{d}\omega'_x}{\mathrm{d}t} = \frac{1}{\omega'_y}\frac{\mathrm{d}\omega'_y}{\mathrm{d}t} \, . \tag{1.10}$$

For $\omega'_x(0) \approx \omega'_y(0)$, this yields the formation of vortex filaments oriented at 45° with respect to the x-direction. As suggested by Tritton (1991, private communication), this results from a balance involving stretching of vorticity, turning of mean flow vorticity by the perturbation and turning of perturbation vorticity by the mean shear (see also Yanase *et al.* 1993).

1.2.2. *The nonlinear regime: the mechanism of weak absolute vorticity stretching*

The previous analysis allows the description of the early, linear stage of the perturbation growth, being based upon a linearization of the governing equations. Further insight into the nonlinear regime can be obtained by examining the vorticity stretching mechanisms. In a previous study (Lesieur, Yanase & Métais 1991), we have emphasized the importance of considering the absolute vorticity, since, in the presence of rotation, Kelvin's theorem directly applies to it. If the viscosity is neglected, absolute vortex filaments are material. We suppose that they will be stretched in a hairpin manner by the ambient shear if the initial absolute vorticity is weak enough, thus producing longitudinal relative vorticity and three-dimensionalization. Let us make this argument precise. The relative vorticity is the sum of the background $-(\mathrm{d}\bar{u}/\mathrm{d}y)z$ and fluctuating $\boldsymbol{\omega}'$ components. The absolute vorticity is then $\left(2\Omega - \mathrm{d}\bar{u}/\mathrm{d}y\right)z + \boldsymbol{\omega}'$. If the flow is locally cyclonic (i.e. Ω and $-\left(\mathrm{d}\bar{u}/\mathrm{d}y\right)$ have the same sign), then the absolute vortex lines are closer to the spanwise direction than the corresponding relative ones, and the absolute vorticity is larger than its relative counterpart. Therefore, as compared to the nonrotating case, the effectiveness of vortex turning and stretching is reduced. Conversely, if the flow is locally anticyclonic, especially for the regions where 2Ω has a value close to $\mathrm{d}\bar{u}/\mathrm{d}y$ (weak absolute spanwise vorticity), absolute vortex lines are very convoluted, and will be rapidly stretched out, as would dye. It was thus suggested that in rotating mixing layers and wakes, the vortex filaments with local Rossby number near -1 (hence anticyclonic) would be stretched into longitudinal alternate vortices. This phenomenological theory will be referred to as the *weak absolute vorticity stretching mechanism.*

In this paper, we present both direct and large-eddy numerical simulations of planar mixing layers and wakes subjected to solid-body rotation with axis perpendicular to the plane of the background flow. The case of temporally growing flows is investigated here. Preliminary results have been obtained concerning spatially growing flows (Métais, Riley & Lesieur 1993), and a more complete study will be presented elsewhere. The numerical methods are presented in § 2. Sections 3 and 4 are devoted to the presentation of the computational results. In § 3, the initial perturbation imposed on the basic velocity profile is quasi-two-dimensional both for the mixing layer and the wake (forced transition). The absolute value of the Rossby number ranges from large (slow rotation) to small (rapid rotation) values. Both cyclonic and anticyclonic cases are investigated. Section 4 focuses on the regime of maximum anticyclonic destabilization. The influences of the initial perturbation (natural or forced) and of the Reynolds number (DNS or LES) are considered. Special attention is given to the coherent-vortex dynamics and stretching mechanisms. The numerical results are interpreted in the light of both the linear-stability analyses and the weak absolute vorticity stretching mechanism. This paper is the second in a series of three papers devoted to the influence of solid-body rotation upon turbulence. In part I (Yanase *et al.* 1993) the linear instability of mixing layers and wakes was studied. Here (part II), we use direct and large-eddy simulations to go beyond the instability theory. In a third paper (Bartello, Métais & Lesieur 1994), the influence of rotation upon initially isotropic turbulence is considered.

2. Numerical methods and governing parameters

2.1. *Governing equations*

The governing equations are the Navier–Stokes and continuity equations written in a Cartesian frame of reference, x, y, z, moving with the rigid-body rotation of angular velocity $\boldsymbol{\Omega} = (0, 0, \Omega)$:

$$\nabla \cdot \boldsymbol{u} = 0\,, \tag{2.1}$$

$$\frac{\partial \boldsymbol{u}}{\partial t} + (\boldsymbol{\omega} + 2\boldsymbol{\Omega}) \times \boldsymbol{u} = -\frac{1}{\rho_0}\nabla\pi + \nu\nabla^2\boldsymbol{u}\,. \tag{2.2}$$

Here $\boldsymbol{u} = (u, v, w)$ and $\boldsymbol{\omega} = (\omega_x, \omega_y, \omega_z)$ are the relative velocity and vorticity vectors. $\pi = p + \frac{1}{2}\rho_0\boldsymbol{u}^2 - \frac{1}{2}\rho_0(\boldsymbol{\Omega}\times\boldsymbol{r})\cdot(\boldsymbol{\Omega}\times\boldsymbol{r})$ corresponds to the modified pressure, with $\boldsymbol{r}$ the position vector, p the static pressure (including gravity) and ρ_0 the (constant) density.

Two prototypes of flows are considered, the mixing layer and the plane wake. For the mixing layer the (initial) mean velocity profile is of hyperbolic-tangent form, i.e.

$$\bar{u}(y) = U_0 \tanh\frac{y}{\delta}\,, \tag{2.3}$$

where $2U_0$ is the velocity difference accross the layer, and $\delta = \delta_i/2$, with δ_i initial vorticity thickness ($\delta_i = 2U_0/|\mathrm{d}\bar{u}/\mathrm{d}y|_{max}$). For the wake, we take a Gaussian mean velocity profile given by

$$\bar{u}(y) = U_0 \exp\left(-\frac{e}{2}\frac{y^2}{\delta^2}\right)\,, \tag{2.4}$$

where U_0 is now the peak deficit velocity. Such a form is justified by the fact that we use a temporal approximation, where the velocity may be reversed and arbitrarily translated. δ is related to the initial half-width r_m through $r_m = (2\ln 2/e)^{1/2}\delta \approx 0.71\delta$. U_o and δ have been defined so that $|U_o|/\delta$ is the magnitude of the maximum initial background vorticity for each case. To be consistent with the companion paper by Yanase *et al.* (1993), we base the characteristic Rossby number on the vorticity extrema associated with the mean velocity profiles. As opposed to the linear stability analysis performed on mean profiles taken independent of time, these, however, vary when solving the full Navier–Stokes equations. Therefore, we here base the characteristic parameters upon the *initial* mean profiles, and mark the corresponding quantities with the superscript (i). Note that, in the initial linear regime, the temporal variations of these profiles remain negligible ahead of the exponential growth of the perturbations. Thus, during that stage, the Rossby number can be considered to be nearly constant and the numerical simulations results can be directly compared with the linear stability analysis. For the mixing layer, the vorticity extremum is given by

$$\omega_{2D}^{(i)} = -\frac{U_0}{\delta} \tag{2.5}$$

such that

$$R_o^{(i)} = \frac{\omega_{2D}^{(i)}}{2\Omega} \ . \tag{2.6}$$

Here, we define $R_o^{(i)}, U_0$ and Ω to be positive or negative, but δ positive. Therefore, $R_o^{(i)}$ is positive for cyclonic rotation (U_0 and Ω of opposite sign) and negative for anticyclonic rotation. The plane wake presents two vorticity extrema,

$$\omega_{2D}^{(i)} = \pm\frac{U_0}{\delta} \ , \tag{2.7}$$

such that $R_o^{(i)}$ given by (2.6) has one sign for $y > 0$ and the opposite sign for $y < 0$. One side of the wake is cyclonic, while the other is anticyclonic. In fact, the results for the wake will be presented in terms of $|R_o^{(i)}| = \left|\omega_{2D}^{(i)}/2\Omega\right|$. The second non-dimensional parameter is the initial Reynolds number,

$$Re^{(i)} = \frac{|U_0|\delta}{\nu} \ . \tag{2.8}$$

More conventionally, the Reynolds number is based on δ_i for the mixing layer and on r_m for the wake; the multiplying factors to recover the conventional notations are respectively 2 and 0.71 (approximately).

2.2. *Numerical methods*

For both flows, periodicity is assumed in the streamwise direction x (the temporal hypothesis) as well as in the spanwise direction y. In these directions, the variables are expanded in Fourier series and a classical collocation method is used. The wake profile given by (2.4) is compatible with periodicity assumptions and the shear direction can be treated similarly to the other two directions. For the mixing layer, in the absence of rotation, it is possible to expand the u and w components of the velocity field in cosine series with respect to y, and v in a sine series. It is not possible to use this procedure in the presence of the Coriolis force. Indeed, the sine series for v leads, in the equations of motion, to sums of terms with cosine symmetry and terms with sine symmetry. To tackle this difficulty, we have simulated a double mixing layer,

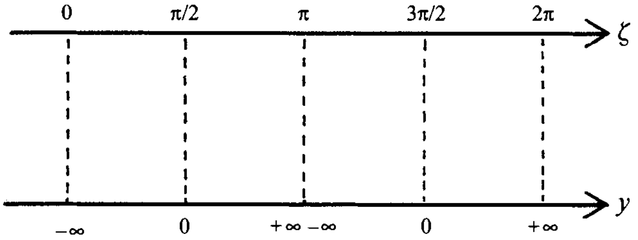

FIGURE 1. Correspondence between the physical space (y-space) and its image (ζ-space).

with both layers extending to infinity in the y-direction. These two infinite spaces can be mapped onto a single interval of finite extent in the computational coordinate ζ (Cain, Ferziger & Reynolds 1984). The cotangent mapping is a suitable mapping function for this purpose:

$$y = h(\zeta) = -b\cot\zeta \ , \tag{2.9}$$

where b is an adjustable constant called *the stretching parameter*. Here we have taken $b = 4$. We let ζ vary in the interval $[0, 2\pi]$ such that the image of the ζ-space corresponds to two infinite regions $-\infty \leqslant y \leqslant +\infty$ (for $\zeta \in [0,\pi[$ and for $\zeta \in]\pi, 2\pi]$, see figure 1). The background velocity field in the ζ-space is defined as

$$U(\zeta) = U_0 \tanh\frac{h(\zeta)}{\delta} \ , \ \text{for } \zeta \in]0,\pi[\ , \tag{2.10}$$

$$U(\zeta) = -U_0 \tanh\frac{h(\zeta)}{\delta} \ , \ \text{for } \zeta \in]\pi,2\pi[\tag{2.11}$$

and completed through continuity in $0, \pi$, and 2π with $U(0) = -U(\pi) = U(2\pi) = U_0$. It is then possible to apply the usual Fourier collocation method in the ζ-direction. Through this procedure, two mixing layers of infinite extent are simultaneously simulated in the y-space; for positive U_0, the vorticity associated with the mean velocity profile of the first one is negative $[\bar{u}(y) = U_0 \tanh y/\delta]$, while it is positive for the second $[\bar{u}(y) = -U_0 \tanh y/\delta]$. When solid-body rotation is imposed, one single run then allows the simultaneous computation a cyclonic mixing layer and also an anticyclonic one of opposite-signed Rossby number.

When used, the large-eddy simulations will be based on the structure-function model (see §4.3; Métais & Lesieur 1992).

2.3. *Initial conditions*

For all the runs, the longitudinal length of the computational domain is equal to twice the wavelength λ_x of the most amplified mode based upon inviscid linear-stability theory, viz. $7.07\delta_i$ for the mixing layer (Michalke 1964), and $7.96r_m$ for the plane wake (Sato & Kuriki 1961). In the case of the wake, the computational domain is cubic. For the mixing layer, the spanwise length of the computational domain is equal to the longitudinal length, while the length in the shear direction extends to infinity.

Initially, a low-amplitude random noise is superposed upon the mean velocity profiles given by (2.3) and (2.4). Several numerical and laboratory experiments have demonstrated the strong influence of initial conditions on the long time evolution of the free-shear flows: see e.g. Comte, Lesieur & Lamballais (1992), for the three-dimensional mixing-layer; Williamson & Prasad (1993), for the plane wake. We have here successively considered two different types of perturbations. First, a quasi-two-dimensional one consisting of the superposition of a purely two-dimensional perturbation (z independent) of kinetic energy $\epsilon_{2D}U_0^2$ and a three-dimensional perturbation of energy $\epsilon_{3D}U_0^2$. For the mixing layer, $\epsilon_{2D} = 10\epsilon_{3D} = 10^{-4}$, and $\epsilon_{2D} = \epsilon_{3D} = 2 \times 10^{-5}$ for the wake. The kinetic energy spectrum for each velocity component is given by

$$E(k) \propto k^8 \exp(-4k^2/k_c^2) \ , \tag{2.12}$$

where $k = ||\boldsymbol{k}||$, corresponding to a narrow-banded spectrum peaking at wavenumber k_c. In this case, $k_c = 2$. Therefore, in the first case the fundamental mode is emphasized, biasing the formation of the Kelvin–Helmholtz vortices of the mixing layer or the wake. This will be referred to as the 'forced transition' case.

The second type of perturbation which has been considered is purely three-dimensional, with $\epsilon_{3D} = 10^{-4}$ and $\epsilon_{2D} = 0$. Now we choose a broad-band spectrum exhibiting, over most of the wavenumbers, a k^2 energy equipartition behaviour

$$E(k) \propto k^2 \exp(-k^2/k_c^2) \ . \tag{2.13}$$

Here, $k_c = 14$. In this case, there is no favoured mode, and the most amplified one can freely emerge. This will be called the 'natural transition' case, where the three-dimensional initial perturbation plays the role of residual turbulence superposed upon the basic flow.

For the wake, the calculations are performed with $64 \times 64 \times 64$ modes in the x-, y-, and z-directions, respectively. $64 \times 128 \times 64$ grid points are used to simulate the double mixing layer. The Reynolds numbers $Re^{(i)} = |U_0|\delta/\nu$ are 50 for the mixing layer and 280 for the wake. The corresponding Reynolds numbers based upon δ_i and r_m are then 100 and 200. For a spatially evolving wake, of upstream velocity U_0 behind a cylinder of diameter $d \approx 2r_m$, this would correspond to a Reynolds number $U_0 d/\nu \approx 400$.

3. Numerical experiments: forced transition

3.1. *The mixing layer*

3.1.1. *Statistics*

The present computations complement and extend those previously performed at lower resolution for the mixing layer by Lesieur *et al.* (1991). In that paper it was shown, in particular, that at $R_o^{(i)} = -0.25$ the effect of rotation is to make the anticyclonic mixing layer less three-dimensional, in agreement with Taylor–Proudman theorem. The same effect occurs at $|R_o^{(i)}| = 0.5$ in a wake (Flores 1993) and in initially quasi-two-dimensional and three-dimensional isotropic turbulence subject to rotation (Bartello *et al.* 1994).

In shear flows, the development of three-dimensional instabilities yields the longitudinal stretching of the vortex filaments by the basic shear. Therefore, the time evolution of the enstrophy associated with the vorticity components perpendicular to the mean flow vorticity $\frac{1}{2}\left\langle \omega_l'^2 \right\rangle = \frac{1}{2}\left\langle \omega_x'^2 + \omega_y'^2 \right\rangle$ represents a good indicator of the flow three-dimensionality (see figure 2). Although it involves the vorticity components both in the shear and streamwise directions, it will be referred to as the 'longitudinal' enstrophy with reference to the so-called longitudinal vortices observed in shear flows. We recall that a prime refers to the perturbed fields. The brackets denote the average over the entire cyclonic side of the computational domain for figure 2(a) and over the entire anticyclonic side for figure 2(b). Direct numerical simulations are performed at $|R_o^{(i)}| = \infty, 20, 10, 5, 2.5, 1$, where $|R_o^{(i)}| = \infty$ denotes the case with no solid-body rotation.

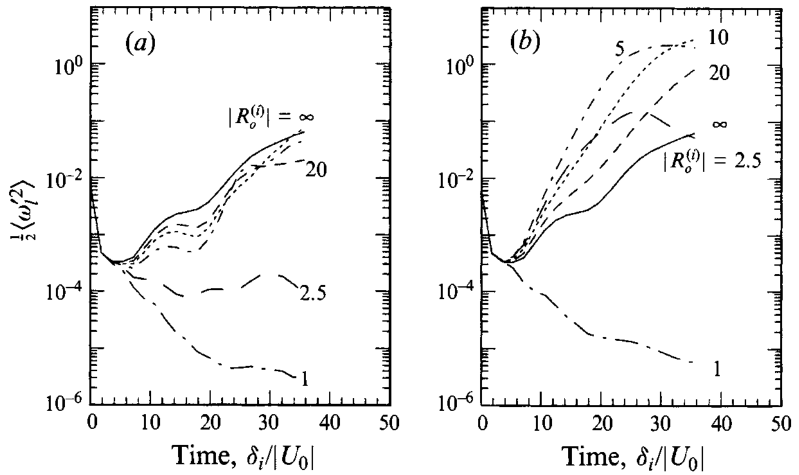

FIGURE 2. Mixing layer. Time evolution of the relative longitudinal vorticity half-variance $\frac{1}{2}\langle\omega_l'^2\rangle = \frac{1}{2}\langle\omega_x'^2 + \omega_y'^2\rangle$ (normalized by $\omega_{2D}^{(i)^2}$) for $|R_o^{(i)}| = \infty, 20, 10, 5, 2.5, 1$. The time unit is $\delta_i/|U_0|$. (*a*) Cyclonic case; (*b*) anticyclonic case.

In the absence of rotation, and after an initial adjustment stage, the stretching mechanisms lead to longitudinal vorticity amplification. This corresponds to the stretching of longitudinal vorticity, especially in the stagnation regions between the Kelvin–Helmholtz vortices. If $\boldsymbol{D}$ is the deformation tensor in this region, in the inviscid case the vorticity satisfies:

$$\frac{\mathrm{d}\omega}{\mathrm{d}t} = \boldsymbol{D} : \omega \ . \tag{3.1}$$

If one assumes that the eigenvectors and eigenvalues of $\boldsymbol{D}$ do not change very much, the longitudinal vorticity will be stretched exponentially in the direction of the first principal axis of deformation, that is, at approximately 45° with respect to the (x,z)-plane.

In the cyclonic case (figure 2*a*), the three-dimensionality is less and less pronounced as the initial Rossby number is decreased from infinity to smaller and smaller values. This is the demonstration that the longitudinal stretching is inhibited by cyclonic rotation. The anticyclonic rotation has an extremely different effect on the longitudinal vorticity developement (figure 2*b*). For $R_o^{(i)} = -20, -10, -5$, and -2.5, the flow is destabilized: the initial growth rate of the longitudinal enstrophy is higher than in the nonrotating case. When the Rossby number goes from -2.5 to -1, there is a sharp transition, since the effect of rotation is again stabilizing. The situation is then very similar to the cyclonic case.

Since small initial perturbations are applied, we examine the early stage of the instability characteristics in the light of linear-stability analysis performed by Yanase *et al.* (1993). The numerical simulations confirm their results: cyclonic rotation as well as strong anticyclonic rotation tend to inhibit three-dimensional motions, whereas weaker anticyclonic rotation ($R_o < -1$) acts to amplify them. The linear analysis shows that the growth of the shear/Coriolis instability mode ($k_x = 0$) is maximum around $R_o \approx -2.5$ and decreases as R_o goes to smaller negative values. As far as the numerical simulations are concerned, the growth rate of the perturbed kinetic energy is initially comparable for $R_o^{(i)} = -2.5$ and $R_o^{(i)} = -5$ (slightly larger in the former case). The nonlinear effects, however, imply a departure from the linear

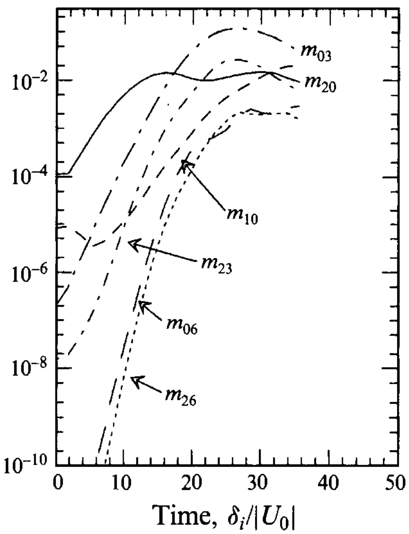

FIGURE 3. Anticyclonic mixing layer at $R_o = -5$. Time evolution of the kinetic energy fluctuations in various spectral modes m_{k_x,k_z}.

predictions, and occur earlier for $R_o^{(i)} = -2.5$. At $R_o^{(i)} = -5$ and $Re^{(i)} = 50$, Yanase *et al.* (1993) have predicted that the maximum shear/Coriolis growth rate takes place for the mode such that $k_{SC} \approx 3k_{KH}$ ($k_x = 0$), where k_{KH} is the wavenumber of the most unstable Kelvin–Helmholtz mode. It was also predicted that its amplification rate would be equal to approximately 1.4 times that of the most unstable Kelvin–Helmholtz mode. Notice that k_{SC} increases with the Reynolds number (see Yanase *et al.* 1993); numerical simulations are therefore constrained to low Reynolds number values in order to properly resolve this mode. For the anticyclonic mixing layer at $R_o = -5$ as given by the numerical simulation, figure 3 shows the time evolution of the kinetic energy fluctuations contained in the various spectral modes, designated by m_{k_x,k_z}, where $m_{2,0}$ is the fundamental (most unstable) Kelvin–Helmholtz mode. An average is performed in the y-direction. The early development is dominated by the Kelvin–Helmholtz mode. The fastest growth is observed for $m_{0,6}$, however, in agreement with the linear-stability analysis. Other longitudinal modes such as $m_{0,3}$ exhibit a strong amplification. The same holds for the oblique modes $m_{2,3}$ and $m_{2,6}$. This eventually leads for $t > 20\ \delta_i/|U_0|$ to a highly nonlinear state with a wide range of excited modes. But the most energetic mode in the final stage becomes the purely longitudinal mode $m_{0,3}$. In the nonlinear regime, the energy is efficiently transferred to smaller scales where viscous dissipation takes place: this yields a saturation of the perturbation growth for $t > 30\ \delta_i/|U_0|$ (see figure 2*b*).

We now examine in detail how rotation selectively affects the time evolution of the two-dimensional and three-dimensional components of the motion as well as the energy transfer between them. For this purpose, we decompose the velocity field fluctuations $u_i'(x,y,z,t)$ into its two-dimensional part $\tilde{u}_i(x,y,t)$, independent of z (obtained by averaging in the z-direction), and its three-dimensional part $u_i^{*}(x,y,z,t)$. The total field is then

$$u_i(x,y,z,t) = \overline{u}_i(y,t) + \tilde{u}_i(x,y,t) + u_i^{*}(x,y,z,t)\ , \tag{3.2}$$

where $\overline{u}_i(y,t)$ is the basic field, the operator $\overline{(\cdot)}$ standing for the average in the x- and z-directions.

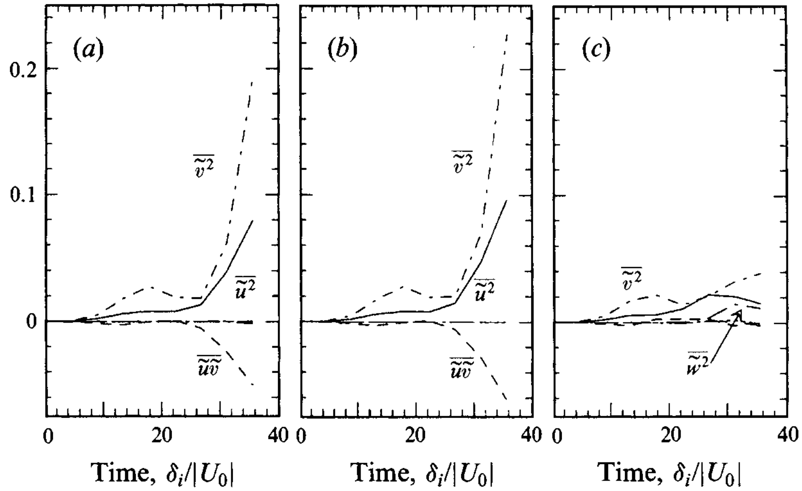

FIGURE 4. Mixing layer. Time evolution of the two-dimensional contribution $\overline{\tilde{u}_i\tilde{u}_j}$ to the Reynolds stress: (*a*) nonrotating case; (*b*) cyclonic case, $R_o^{(i)} = 5$; (*c*) anticyclonic case, $R_o^{(i)} = -5$.

We first consider the time evolution of the Reynolds stress components. One can show that

$$\overline{u'_i u'_j} = \overline{(\tilde{u}_i + u_i^*)(\tilde{u}_j + u_j^*)} = \overline{\tilde{u}_i\tilde{u}_j} + \overline{u_i^* u_j^*}. \tag{3.3}$$

Figure 4 displays the time evolution of the two-dimensional contribution $\overline{\tilde{u}_i\tilde{u}_j}$ to the Reynolds stress. The nonrotating case (figure 4*a*) is compared to the cyclonic and anticyclonic cases (figures 4*b* and 4*c*) corresponding respectively to $R_o^{(i)} = 5$ and -5. In the nonrotating case, the most significative components are $\overline{\tilde{u}^2}$, $\overline{\tilde{v}^2}$ and $\overline{\tilde{u}\tilde{v}}$. Both for cyclonic and anticyclonic rotation, the components of the two-dimensional stress are weakly affected by the rotation for $t < 25\delta_i/|U_0|$. Afterwards, their growth is inhibited in the anticyclonic case, except for $\overline{\tilde{w}^2}$, which exhibits larger values than in the nonrotating case. Conversely, the stress components are enhanced by the cyclonic rotation, except $\overline{\tilde{w}^2}$ which is now reduced; this clearly shows a tendency of flow to become more two-dimensional.

The effects are dramatically different when the three-dimensional components $\overline{u_i^* u_j^*}$ of the stress are considered (see figure 5). Since the initial conditions are quasi-two-dimensional, the three-dimensional stress components are slightly smaller than the two-dimensional ones in the nonrotating case. The trend toward two-dimensionalization in the cyclonic case is confirmed by the total inhibition of the three-dimensional stress components. On the other hand, these are considerably amplified by a moderate anticyclonic rotation.

The equations governing the kinetic energy evolution for each of the components $\bar{u}$, $\tilde{u}$ and u^* involve various contributions to the energetic transfer. Among those, we here consider

$$T_{m2} = -\int_{\mathscr{D}} \overline{\tilde{u}_j\tilde{u}_i}\frac{\partial \bar{u}_i}{\partial x_j}\,\mathrm{d}y\ , \tag{3.4}$$

$$T_{m3} = -\int_{\mathscr{D}} \overline{u_j^* u_i^*}\frac{\partial \bar{u}_i}{\partial x_j}\,\mathrm{d}y\ , \tag{3.5}$$

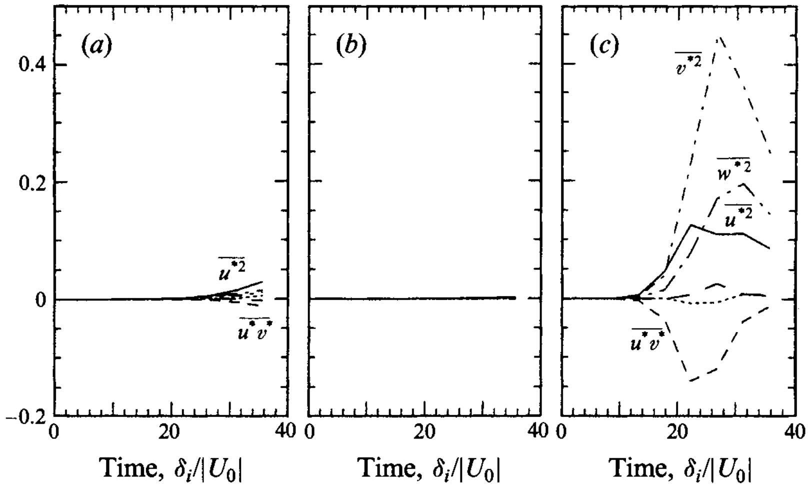

FIGURE 5. Same as figure 4 but for the three-dimensional components $\overline{u_i^* u_j^*}$ of the Reynolds stress.

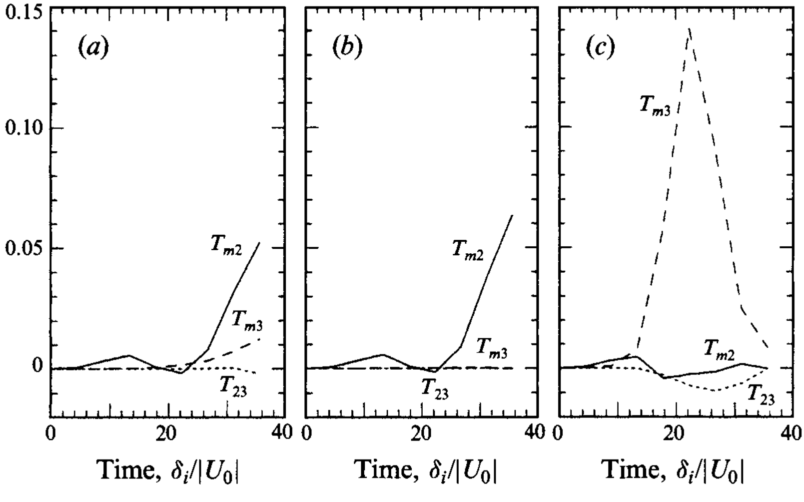

FIGURE 6. Mixing layer. Time evolution of T_{m2}, T_{m3} and T_{23} (see (3.4); (3.5); (3.6)): (*a*) $R_o^{(i)} = \infty$; (*b*) $R_o^{(i)} = 5$ (cyclonic); (*c*) $R_o^{(i)} = -5$ (anticyclonic).

$$T_{23} = -\int_{\mathscr{D}} \overline{u_j^* u_i^* \frac{\partial \tilde{u}_i}{\partial x_j}}\, \mathrm{d}y\,, \tag{3.6}$$

where $\int_{\mathscr{D}}(\cdot)\mathrm{d}y$ designates the integral over the whole y extent of the cyclonic or anticyclonic side of the computational domain $\mathscr{D}$. A positive value for T_{m2} signifies an energy transfer from the mean flow to the two-dimensional component of the motion. Similarly, the energy is transferred from the mean flow to the three-dimensional component when $T_{m3} > 0$, and from the two-dimensional to the three-dimensional component when $T_{23} > 0$. Figure 6 represents the time evolution of T_{m2}, T_{m3} and T_{23} for the three cases: (*a*) $R_o^{(i)} = \infty$; (*b*) $R_o^{(i)} = 5$ (cyclonic); (*c*) $R_o^{(i)} = -5$ (anticyclonic). In the non-rotating case, the energy transfer is mainly directed from the mean flow to the two-dimensional component (Kelvin–Helmholtz vortices). The three-dimensional part of the motion only extracts a weak portion of the mean flow energy. This corresponds to the stretching of hairpin vortices by the basic shear. In the cyclonic mixing layer, the latter exchange is completely inhibited, and the energy exchanges are preferably directed from the mean flow to the two-dimensional component of the motion, corresponding to an enhancement of T_{m2}. By contrast, for anticyclonic rotation, the flow is rendered much more three-dimensional: the energy tranfer is mainly directed from the mean flow to the three-dimensional motion, and very little is transferred to the two-dimensional part. This indicates a very intense stretching of longitudinal vorticity by the basic shear, and the disappearance of two-dimensional Kelvin–Helmholtz vortices.

3.1.2. *Coherent vortices*

Now we look at the three-dimensional flow structure. We focus on the relative vorticity iso-surfaces at $t = 17.8\delta_i/|U_0|$ obtained in the nonrotating case ($R_o^{(i)} = \infty$), and for anticyclonic rotation at $R_o^{(i)} = -5$ and $R_o^{(i)} = -1$.

(i) $R_o^{(i)} = \infty$. Figure 7(*a*) shows the iso-contours of spanwise vorticity corresponding to 45% of $|\omega_{2D}^{(i)}|$, where $\omega_{2D}^{(i)}$ is the maximum vorticity associated with the initial mean velocity profile (see (2.5)). Here, one observes quasi-two-dimensional Kelvin–Helmholtz billows, slightly distorted in the spanwise direction. Weak longitudinal vortices are stretched between the primary rolls; these are identified by observing isosurfaces of longitudinal vorticity $\omega_l = (\omega_x^2 + \omega_y^2)^{1/2}$ corresponding to the very low value of about 4.5% of $|\omega_{2D}^{(i)}|$. This longitudinal vortex stretching increases with increasing Reynolds number, as has been checked using DNS. LES also allows the very efficient stretching of the longitudinal vorticity (see below).

(ii) $R_o^{(i)} = -1$. Figure 7(*b*) displays the spanwise vorticity field with the same iso-contour value as in the nonrotating case. Anticyclonic and cyclonic flows are similar at this Rossby number, as a strong two-dimensionalization is observed in both cases. The longitudinal vortices have disappeared. In addition, the tendency towards two-dimensionality can be observed in the cyclonic case even for large positive $R_o^{(i)}$.

(iii) $R_o^{(i)} = -5$. The Kelvin–Helmholtz vortices are highly distorted and exhibit strong oscillations along the spanwise direction (see figure 7*c*). The longitudinal vorticity is much higher than in the nonrotating case, and the two Kelvin–Helmholtz rolls are linked with longitudinal hairpin vortices shown here by the isosurfaces at 22.5% of $|\omega_{2D}^{(i)}|$. Figure 8 shows a time sequence of isosurfaces of the relative vorticity modulus at $t = 17.8$ (figure 8*a*), $t = 22.3$ (figure 8*b*) and $t = 26.8\delta_i/|U_0|$ (figure 8*c*). The first picture is similar to figure 7(*c*) but the iso-contours are different; we see the simultaneous formation of Kelvin–Helmholtz vortices and longitudinal hairpin vortices which are stretched in between. As time goes on, this produces a significant increase of the longitudinal component of the vorticity. By the end of the run (figure 8*c*), the Kelvin–Helmholtz vortices have been totally dislocated and the flow is entirely composed of hairpin-shaped longitudinal vortices. A similar sequence had been proposed in this case by Lesieur *et al.* (1991), using the weak absolute vorticity stretching mechanism: weak absolute vorticity in the stagnation region between the Kelvin–Helmholtz rollers would be stretched longitudinally between the latter, yielding longitudinal alternate vortices which should destroy the primary vortices. One can notice that the spanwise wavelength of the vortices is one third of the spanwise extent of the computational domain. This corresponds to the growth of the $m_{0,3}$ mode already observed in figure 3. More details on the formation mechanisms of these vortices will be given in §4.

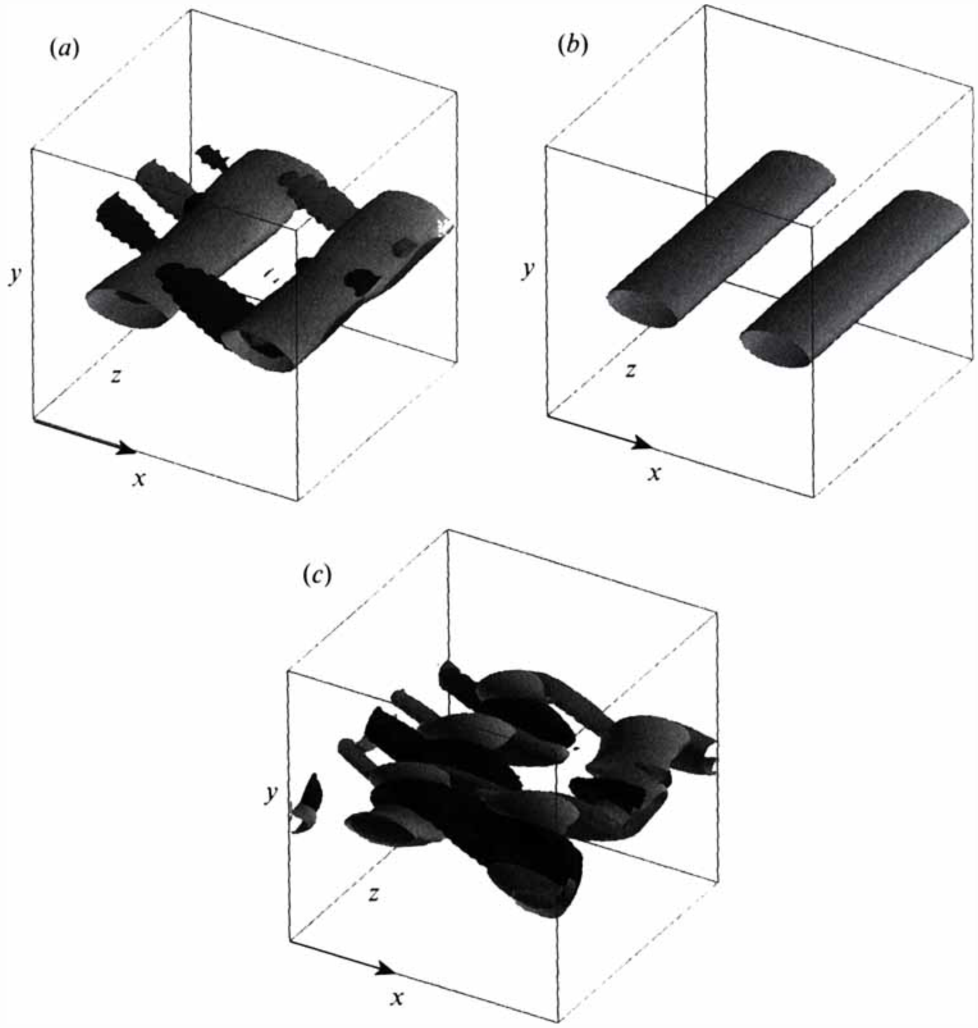

FIGURE 7. Mixing layer. Relative vorticity isosurfaces at $t = 17.8\delta_i/|U_0|$. (*a*) Nonrotating case: $\omega_z = 45\%$ of $|\omega_{2D}^{(i)}|$, light gray; $\omega_l = 4.5\%$ of $|\omega_{2D}^{(i)}|$ coloured by the sign of ω_x, black $\omega_x < 0$, dark gray $\omega_x > 0$. (*b*) $R_o^{(i)} = -1$: $\omega_z = 45\%$ of $|\omega_{2D}^{(i)}|$, light gray. (*c*) $R_o^{(i)} = -5$: $\omega_z = 45\%$ of $|\omega_{2D}^{(i)}|$, light gray; $\omega_l = 22.5\%$ of $|\omega_{2D}^{(i)}|$ coloured by the sign of ω_x, black $\omega_x < 0$, dark gray $\omega_x > 0$.

3.2. *The plane wake*

3.2.1. *Statistics*

Cyclonic and anticyclonic vortices are now simultaneously present within the computational domain. Figure 9 is the analogue of figure 2 for the case of the wake: $\frac{1}{2}\left\langle \omega_l'^2 \right\rangle$ designates a spatial average of the fluctuating longitudinal enstrophy over the points of the computational domain at which the total relative spanwise vorticity is positive (cyclonic) for figure 9(*a*) and negative (anticyclonic) for figure 9(*b*). The Rossby numbers considered here are $|R_o^{(i)}| = \infty$, 7, 2.5, 1.3 and 0.5. On the anticyclonic side, the time evolution of $\frac{1}{2}\left\langle \omega_l'^2 \right\rangle$ exhibits similar features to those observed for the

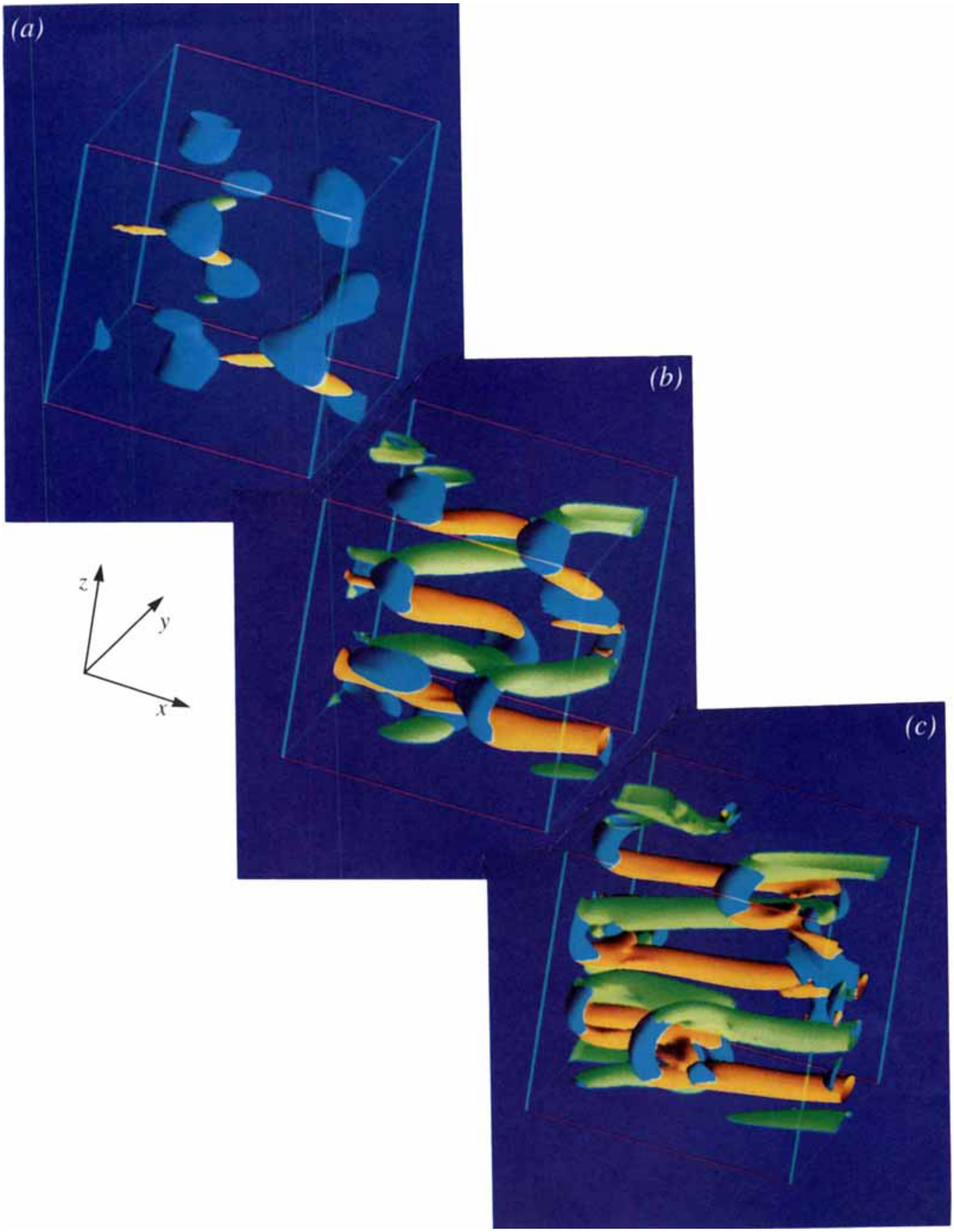

FIGURE 8. Anticyclonic mixing layer at $R_o^{(i)} = -5$. Relative vorticity isosurfaces at: (*a*) $t = 17.8$; (*b*) $t = 22.3$; (*c*) $t = 26.8\delta_i/|U_0|$. $\omega_z = 45\%$ of $|\omega_{2D}^{(i)}|$, blue; $\omega_l = 45\%$ of $|\omega_{2D}^{(i)}|$ coloured by the sign of ω_x, orange $\omega_x < 0$, green $\omega_x > 0$.

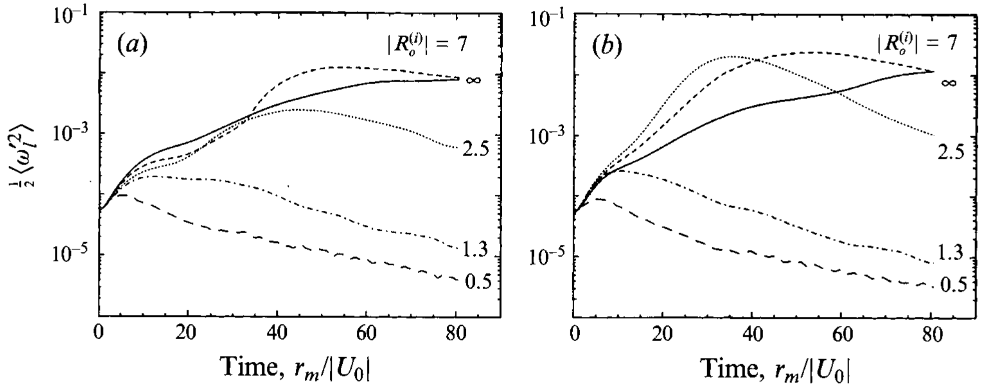

FIGURE 9. Plane wake. Time evolution of the relative longitudinal vorticity half-variance $\frac{1}{2}\langle\omega_l'^2\rangle = \frac{1}{2}\langle\omega_x'^2+\omega_y'^2\rangle$ (normalized by $\omega_{2D}^{(i)2}$) for $|R_o^{(i)}| = \infty$, 7, 2.5, 1.3 and 0.5. The time unit is $r_m/|U_0|$. Spatial average over the points of the computational domain at which the total relative spanwise vorticity is positive (cyclonic) for (*a*) and negative (anticyclonic) for (*b*).

anticyclonic mixing layer. For $|R_o^{(i)}| = 7$ and 2.5, the perturbation rapidly grows in the initial stages, then saturates and eventually decreases. The maximum anticyclonic three-dimensionalization occurs at $|R_o^{(i)}| = 2.5$. On the cyclonic side (figure 9*a*), the rotation is initially stabilizing for all simulated values of the Rossby number. Later on, for $|R_o^{(i)}| = 7$ and 2.5, the instantaneous growth of $\frac{1}{2}\left\langle\omega_l'^2\right\rangle$ is stronger than that observed without rotation. This is probably due to the strong three-dimensionalization of the anticyclonic side of the wake, causing the spanwise vorticity to locally change its sign and become cyclonic. These regions then contribute to the 'cyclonic' longitudinal vorticity variance. Furthermore, as shown below, the cyclonic eddies of the Kármán street become more three-dimensional than in the nonrotating case because of their interaction with the highly three-dimensional anticyclonic ones. For $|R_o^{(i)}| = 0.5$, oscillations are observed which may indicate inertial wave propagation.

The linear-stability analysis of the planar wake performed by Yanase *et al.* (1993) gives a maximum destabilization effect for $|R_o^{(i)}| \approx 2.5$. The overall maximum growth rate of the shear/Coriolis instability in this case (for $Re^{(i)} \approx 280$) was observed for $k_{SC} \approx 3.3k_K$, where k_K corresponds to the fundamental (most unstable) Kármán mode. The nonlinear simulation shows good agreement with the linear prediction as far as the Rossby number of maximum destabilization is concerned. Figure 10 exhibits the time evolution of the kinetic energy in the various m_{k_x,k_z} modes averaged over the entire y-direction (both the cyclonic and anticyclonic sides) for the case $|R_o^{(i)}| = 2.5$. In our computation, $m_{2,0}$ is the fundamental Kelvin–Helmholtz mode of the Kármán street. Therefore, $m_{0,6}$ roughly corresponds to the most amplified shear/Coriolis instability mode predicted by the linear-stability analysis. The fastest initial growth is indeed observed for this mode. Owing to the nature of the initial perturbation, however, $m_{0,4}$ dominates all the other longitudinal modes during the entire evolution. It ultimately reaches an energy level comparable with the fundamental mode $m_{2,0}$ and its subharmonic $m_{1,0}$. As in the mixing layer case, several oblique modes such as $m_{2,4}$ are also quickly excited, leading to a highly nonlinear regime.

To address the issue of flow two-dimensionalization by the rotation, we next consider the dependence of the kinetic energy spectrum on the spanwise wavenumber k_z (see figure 11). We compare here, at $t = 48.4\ r_m/|U_0|$, the spectra obtained in

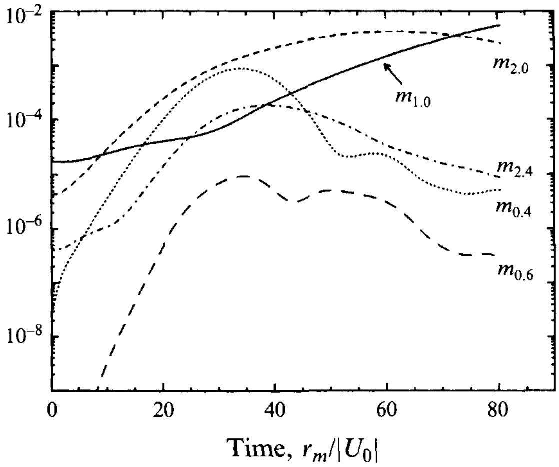

FIGURE 10. Plane wake at $|R_o^{(i)}| = 2.5$. Time evolution of the kinetic energy in the various $m_{k_x k_z}$ modes averaged over the entire y-direction (both the cyclonic and anticyclonic sides).

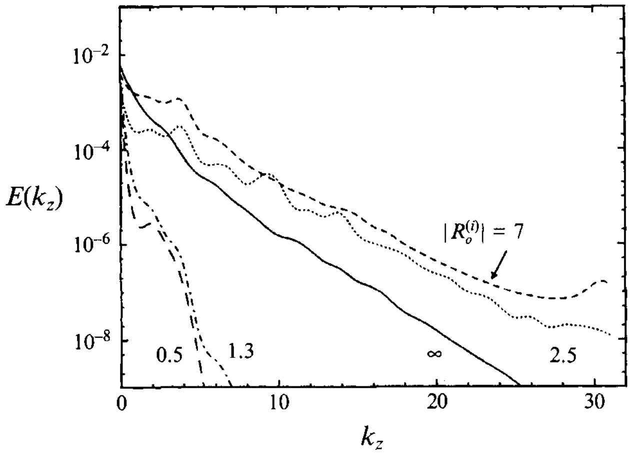

FIGURE 11. Plane wake at $|R_o^{(i)}| = 2.5$. Kinetic energy spectrum versus the spanwise wavenumber k_z at $t = 48.4 r_m/|U_0|$ and $|R_o^{(i)}| = \infty, 7, 2.5, 1.3$ and 0.5.

the nonrotating case, and in the rotating cases for $|R_o^{(i)}| = 7, 2.5, 1.3$ and 0.5. An average is performed in the x- and the entire y- (cyclonic and anticyclonic) directions. In the destabilized cases ($|R_o^{(i)}| = 7$ and 2.5), the wake exhibits significantly more energy at the large k_z wavenumbers than in the nonrotating case. As the Rossby number is decreased from 7 to 0.5, however, the energy spectrum is more and more confined around the wavenumber $k_z = 0$; this shows a clear trend towards flow two-dimensionalization, again displaying consistency with the Taylor–Proudman theorem.

3.2.2. *Coherent vortices*

Similarly to the mixing layer case, we concentrate on relative vorticity iso-surfaces. We consider here the vortices late in their evolution, at $t = 48.4\ r_m/|U_0|$, for the nonrotating case, and for the rotating cases corresponding to $|R_o^{(i)}| = 2.5$ and $|R_o^{(i)}| = 0.5$.

(i) $|R_o^{(i)}| = \infty$. Figure 12(*a*) displays the iso-contours of spanwise vorticity corresponding to $\pm 50\%$ of $|\omega_{2D}^{(i)}|$, where $\omega_{2D}^{(i)}$ is defined in (2.7). The Reynolds number is higher than for the mixing layer computation, presented in the previous section; here $Re^{(i)} = 280$. Furthermore, the initial noise is less two-dimensional with a higher relative amplitude of the three-dimensional part. Since the computational domain length is twice the most amplified wavelength predicted by the linear-stability analysis, the Kármán street consists of two pairs of alternate-sign vortices. Owing to less important viscous effects, the spanwise oscillations of these quasi-two-dimensional billows are more pronounced. The strong three-dimensionality yields the stretching of longitudinal vortices. These are located within the braids connecting consecutive Kármán vortices of anti-parallel vorticity and have an intensity comparable with the latter. These longitudinal structures are identified through isosurfaces of longitudinal vorticity equal to 50% of $|\omega_{2D}^{(i)}|$. The influence of viscosity on the stretching mechanisms will be discussed in § 4, through comparisons of the present direct numerical simulations with large-eddy simulations.

(ii) $|R_o^{(i)}| = 2.5$. Figures 12(*b*) and 12(*c*) show, at an identical time, the same vorticity component iso-contours as in the nonrotating case. As demonstrated by the statistics, this case corresponds to maximum anticyclonic destabilization. Spanwise oscillations of the two cyclonic Kármán-street vortices are induced; these remain linked by an oscillating sheet of spanwise vorticity (see figure 12*b*). On the anticyclonic side, one observes intense hairpin vortices analogous to the ones observed in the anticyclonic mixing layer (see figure 8*c*). Their spanwise wavelength here is one-fourth of the spanwise extent of the computational domain. The anticyclonic Kármán vortices have disappeared.

(iii) $|R_o^{(i)}| = 0.5$. Now the high rotation rate has reorganized the wake into two-dimensional, alternating-signed vortices, and the hairpin vortices are no longer identifiable. We plot in figure 12(*d*) iso-contours of the relative vorticity modulus $||\boldsymbol{\omega}|| = (\omega_x^2 + \omega_y^2 + \omega_z^2)^{1/2}$ corresponding to 50% of $|\omega_{2D}^{(i)}|$. The isosurfaces are coloured by the value of the pressure P, where P includes the centrifugal acceleration, i.e.

$$P = p - \frac{\rho_0}{2}\Omega^2 r^2 \ , \tag{3.7}$$

where $r^2 = x^2 + y^2$. Figure 12(*d*) is compatible with a geostrophic balance, since anticyclonic vortices are pressure highs while cyclones are pressure troughs.

4. Numerical experiments: maximum anticyclonic destabilization

In the present section, special care is given to the coherent-vortex dynamics for rotation rates corresponding to the maximum anticyclonic destabilization. We concentrate both on the anticyclonic mixing layer at $R_o^{(i)} = -5$, and on the wake at $|R_o^{(i)}| = 2.5$. The previous section has demonstrated that for these Rossby numbers, the flow in the anticyclonic regions eventually consists of elongated hairpin vortices stretched in the longitudinal direction. We here concentrate on the generation mechanisms of these vortices.

4.1. *Forced transition*

During the course of time evolution of the mixing layer, the highest values reached for ω_x' and ω_y' are 2.4 $|\omega_{2D}^{(i)}|$ and 1.3 $|\omega_{2D}^{(i)}|$, respectively, indicating an intense longitudinal vorticity stretching. We have checked that the legs of the hairpin vortices of the anticyclonic mixing layer presented in figure 8(*c*) are oriented at an angle

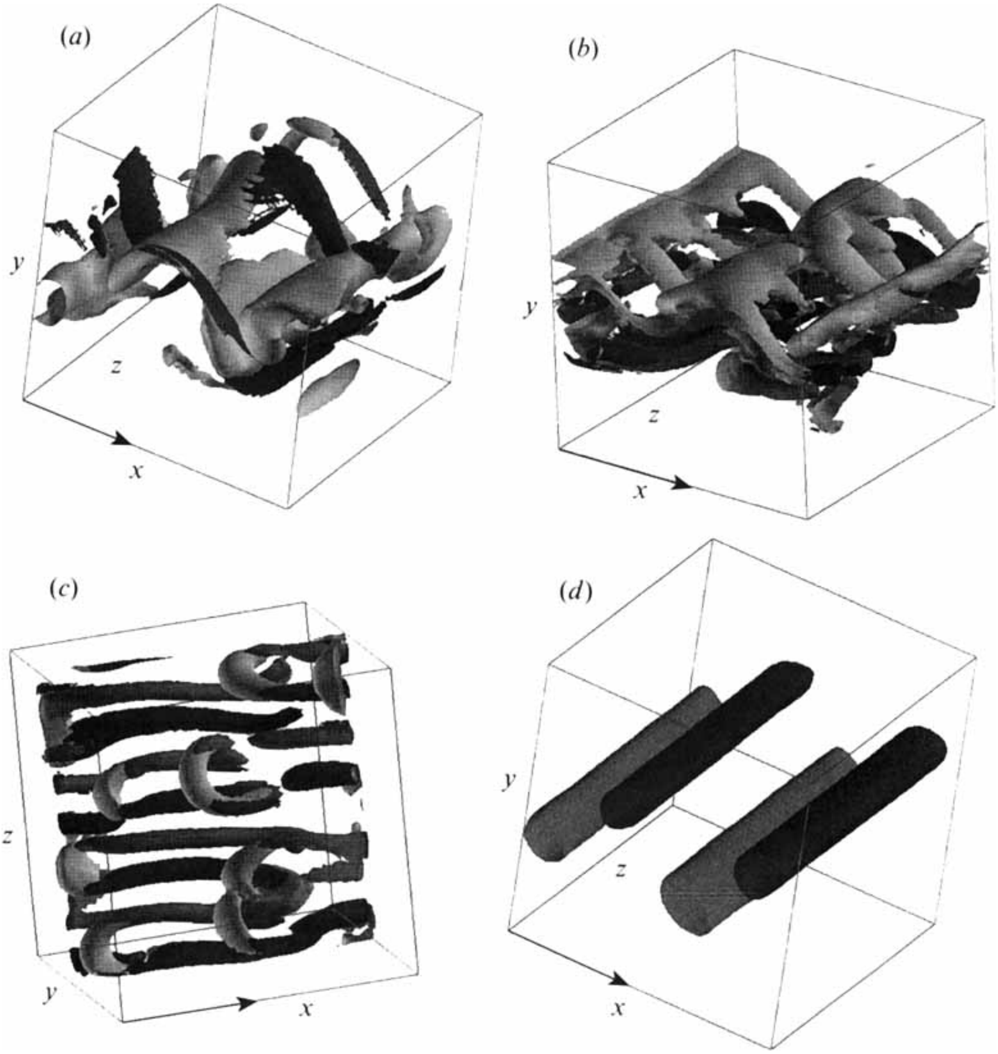

FIGURE 12. Plane wake. Relative vorticity iso-surfaces at $t = 48.4 r_m/|U_0|$. (*a*) Nonrotating case: $\omega_z = \pm 50\%$ of $|\omega_{2D}^{(i)}|$, light gray; $\omega_l = 50\%$ of $|\omega_{2D}^{(i)}|$ coloured by the sign of ω_x, black $\omega_x < 0$, dark gray $\omega_x > 0$. (*b,c*) $|R_o^{(i)}| = 2.5$, same isosurfaces as in (*a*): (*b*) view from the cyclonic side; (*c*) view of the anticyclonic side only. (*d*) $|R_o^{(i)}| = 0.5$. Isosurface $||\vec{\omega}|| = 50\%$ of $|\omega_{2D}^{(i)}|$ coloured by the pressure P (see (3.7)): black, low pressure; dark gray, high pressure.

of approximately 30° with respect to the (x,z)-plane. By comparison, the vorticity maxima in the nonrotating case are only $0.4\,|\omega_{2D}^{(i)}|$ and $0.3\,|\omega_{2D}^{(i)}|$ for ω'_x and ω'_y respectively. The maxima attained for the wake at $|R_o^{(i)}| = 2.5$ are of the same order as for the rotating mixing layer: $2.2\,|\omega_{2D}^{(i)}|$ for ω'_x and $1.4\,|\omega_{2D}^{(i)}|$ for ω'_y. For the nonrotating case $\omega'^{max}_x \approx \omega'^{max}_y \approx 1.8\,|\omega_{2D}^{(i)}|$, indicating that the nonrotating wake is far more three-dimensional than the nonrotating mixing layer. This maximum in the nonrotating wake case is attained at the end of the evolution at $t = 80\ r_m/|U_0|$ (see figure 17*a*), however, while at $|R_o^{(i)}| = 2.5$, the longitudinal stretching is maximum at $t = 35\ r_m/|U_0|$, and is subsequently followed by a decay (see figure 17*a*).

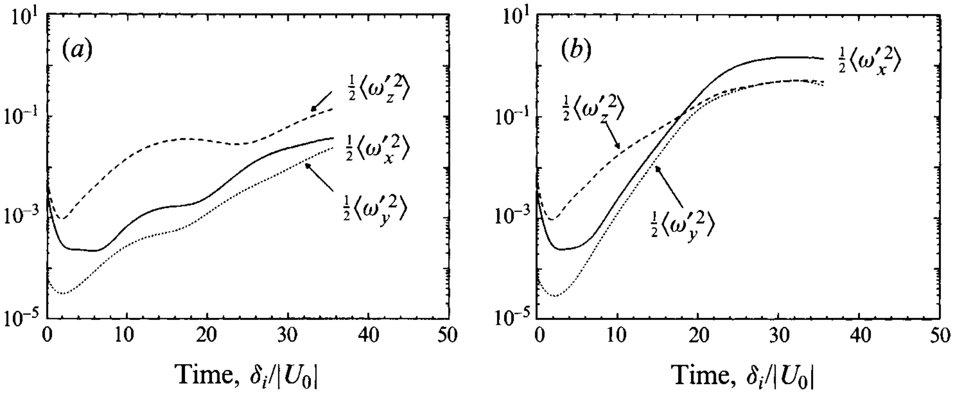

FIGURE 13. Mixing layer, forced transition. Time evolution of the half-variance of the vorticity fluctuation components $\frac{1}{2}\left\langle\omega_x'^2\right\rangle, \frac{1}{2}\left\langle\omega_y'^2\right\rangle$, and $\frac{1}{2}\left\langle\omega_z'^2\right\rangle$ (normalized by $\omega_{2D}^{(i)^2}$). (*a*) Nonrotating case; (*b*) $R_o^{(i)} = -5$.

For the wake, it seems then that rotation first vigorously enhances the anticyclonic longitudinal stretching, but then this mechanism is weakened.

Figure 13 compares the time evolutions of half the variance of the vorticity fluctuation components for the nonrotating (figure 13*a*) and the anticyclonic ($R_o^{(i)} = -5$; figure 13*b*) mixing layer cases. In the absence of rotation, due to the quasi-two-dimensional nature of the mixing layer, $\frac{1}{2}\left\langle\omega_z'^2\right\rangle$ prevails over the other two components during the whole run. The results are significantly different when anticyclonic rotation is imposed. Indeed, for $t \geqslant 8\delta_i/|U_0|$ both $\frac{1}{2}\left\langle\omega_x'^2\right\rangle$ and $\frac{1}{2}\left\langle\omega_y'^2\right\rangle$ undergo a similar exponential growth until $t \approx 20\delta_i/|U_0|$. Afterwards, a nonlinear saturation is observed which occurs at a lower level for the y-component than for the x-component: in the final stage, the latter dominates the flow and

$$\frac{\left\langle\omega_x'^2\right\rangle}{\left\langle\omega_y'^2\right\rangle} \approx \frac{\left\langle\omega_x'^2\right\rangle}{\left\langle\omega_z'^2\right\rangle} \approx 3.1 \quad . \tag{4.1}$$

Similar conclusions can be drawn from the wake computation.

4.2. *Natural transition*

In the 'forced transition' case, the nature of the initial perturbation favours the appearance of the Kelvin–Helmholtz mode. We now consider the 'natural transition' and we investigate which modes are naturally selected: for the wavenumber range $k < 14$, the initial energy perturbation is equally partitioned between all wavenumbers. We first consider in figure 14 the growth of the kinetic energy contained in the various spectral modes for the anticyclonic mixing layer at $R_o^{(i)} = -5$. The picture is somewhat different than in the 'forced transition' case corresponding to figure 3. From the beginning, the fastest growing mode $m_{0,6}$ dominates the flow until $t = 30\ \delta_i/|U_0|$. Subsequently, the energy in this mode saturates and the subharmonic mode $m_{0,3}$ prevails. Here again, by late time, the energy is partitioned over a wide range of modes. Owing to the dominating role played by the fastest growing mode $m_{0,6}$, the flow is now entirely composed of purely longitudinal vorticity structures as shown on figure 15. The absence of the Kelvin–Helmholtz vortices implies, however, a less important longitudinal stretching than in the 'forced transition' case: the highest

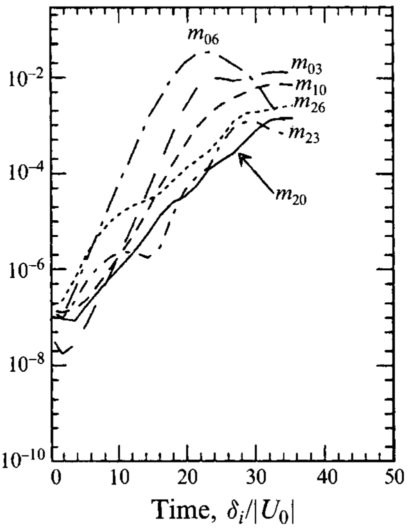

FIGURE 14. Anticyclonic mixing layer at $R_o^{(i)} = -5$, natural transition. Time evolution of the kinetic energy fluctuations in various spectral modes m_{k_x,k_z}.

values for the maxima are now 1.4 $|\omega_{2D}^{(i)}|$ and 0.9 $|\omega_{2D}^{(i)}|$ for ω'_x and ω'_y respectively. The larger amplitude of the stretching terms for ω'_x than for ω'_y (and ω'_z) is confirmed by the time evolution of the averaged quantities $\frac{1}{2}\left\langle\omega'^2_x\right\rangle$, $\frac{1}{2}\left\langle\omega'^2_y\right\rangle$, and $\frac{1}{2}\left\langle\omega'^2_z\right\rangle$ (see figure 16). As in the 'forced transition case', the x- and y-components undergo a similar evolution in the early stage of the development (until $t \approx 14\delta_i/|U_0|$). Later on, all components reach a saturation level and $\left\langle\omega'^2_x\right\rangle$ clearly prevails over the other two components. By the end of the evolution, one obtains

$$\frac{\left\langle\omega'^2_x\right\rangle}{\left\langle\omega'^2_y\right\rangle} \approx \frac{\left\langle\omega'^2_x\right\rangle}{\left\langle\omega'^2_z\right\rangle} \approx 5.3 \quad . \tag{4.2}$$

We have checked that the anticyclonic side of the wake in natural transition at $|R_o^{(i)}| = 2.5$ exhibits similar behaviour, with the same longitudinal structures.

4.3. *Large-eddy simulations (LES)*

In order to investigate the influence of the Reynolds number on vorticity production, LES are performed. We designate as $\bar{a}(\boldsymbol{x})$ the large-scale (grid-scale) component of any quantity $a(\boldsymbol{x})$, and $a' = a - \bar{a}$ the subgrid-scale part. The large-scale velocity field $\bar{u}(\boldsymbol{x},t) = (\bar{u}_1, \bar{u}_2, \bar{u}_3)$ satisfies the filtered Navier–Stokes equations, where the viscous terms in eq. (2.2) are replaced by

$$\frac{\partial}{\partial x_j}\left\{(\nu + \nu_t(\boldsymbol{x},t))\left(\frac{\partial \bar{u}_i}{\partial x_j} + \frac{\partial \bar{u}_j}{\partial x_i}\right)\right\}. \tag{4.3}$$

In addition, the modified pressure $\bar{\pi}$ is now given by

$$\bar{\pi} = \bar{p} + \tfrac{1}{2}\rho_0\bar{u}^2 - \tfrac{1}{2}\rho_0(\boldsymbol{\Omega}\times\boldsymbol{r})\cdot(\boldsymbol{\Omega}\times\boldsymbol{r}) - \tfrac{1}{3}\rho_0 R_{kk} \ , \tag{4.4}$$

R_{ij} being the total subgrid-scale Reynolds stress tensor:

$$R_{ij} = -\left(\overline{\bar{u}_i u'_j} + \overline{u'_i \bar{u}_j} + \overline{u'_i u'_j}\right) \quad . \tag{4.5}$$

For the space-varying eddy viscosity $\nu_t(\boldsymbol{x},t)$ in (4.3), we here choose the *structure-function model* proposed by Métais & Lesieur (1992). The local eddy viscosity is then given by

$$\nu_t(\boldsymbol{x},t) = 0.105\ C_k^{-3/2}\ \Delta x\ \left[\overline{F}_2(\boldsymbol{x},\Delta x,t)\right]^{1/2}\quad . \tag{4.6}$$

$\overline{F}_2(\boldsymbol{x},\Delta x,t)$ is the filtered second-order velocity structure function, Δx is the numerical mesh size, and C_k is the Kolmogorov constant taken equal to 1.4.

We here concentrate on the plane wake. Direct numerical simulations in the forced and natural transition cases are compared to large-eddy simulations with identical initial conditions. For the LES, the kinematic viscosity ν in (4.3) is zero ('infinite' Reynolds number). For all the initial conditions tested, the amplification of the longitudinal vorticity is found to be more important in the LES than in the DNS (see figure 17*a* for the forced transition and figure 17*b* for the natural transition cases). This is true both in the presence of destabilizing rotation (here at $|R_o^{(i)}| = 2.5$), and without any rotation. In the nonrotating case, both in the forced and natural transition, the LES yield $\omega_x'^{max} \approx \omega_y'^{max} \approx 4.8|\omega_{2D}^{(i)}|$. Because of the strong small-scale three-dimensionalization of the wake, the maximum reached by the z-component is of the same order. In the rotating case, the anticyclonic side of the flow is ultimately dominated by ω_x', similar to results in the direct numerical simulation. In the forced transition, ω_x' undergoes a slightly higher stretching than during natural transition. This leads to $\omega_x'^{max}$ approximately $5|\omega_{2D}^{(i)}|$ in the first case, and approximately $4.2|\omega_{2D}^{(i)}|$ in the second case.

The influence of the subgrid-scale model on the early time, weakly nonlinear evolution may be investigated by considering the kinetic energy in the longitudinal modes corresponding to maximum shear/Coriolis instability. Figure 18 shows, in the natural transition case, the temporal evolution of the kinetic energy (integrated over the entire y-direction) within the $m_{0,5}$ and $m_{0,6}$ spectral modes; direct and large-eddy simulations are compared. We recall that $m_{0,6}$ is the fastest growing mode predicted by the linear-stability analysis at $Re^{(i)} = 280$. In the initial stage, both spectral modes exhibit faster exponential growth in the LES case, and nonlinear saturation is observed at earlier time. The maximum energy level reached for these particular modes, however, is of the same order in the viscous (DNS) and 'inviscid' (LES) cases.

As pointed out by Métais & Lesieur (1992), in large-eddy simulations, low-pressure centres are better tracers of the coherent structures than high-vorticity regions, which are encumbered by small-scale structures. Contours of low $\overline{P}(\boldsymbol{x},t)$, with

$$\overline{P}(\boldsymbol{x},t) = \overline{\pi} - \tfrac{1}{2}\rho_0\overline{u}^2 \tag{4.7}$$

and $\overline{\pi}$ given by (4.4) are displayed on figure 19 for the nonrotating plane wake at $t = 65.5r_m/|U_0|$. Figure 19(*a*) corresponds to the large-eddy simulation of forced transition, and figures 19(*b*) and 19(*c*) to natural transition. Pressure troughs indicate not only the primary vortices of the Kármán street, but also the longitudinal vortices between them. As shown in figure 17(*a*), intense longitudinal vorticity stretching takes place. This implies strong depressions. In the natural transition case (see figures 19*b* and 19*c*), the longitudinal vortices exhibit a lambda-shaped structure with a characteristic arrangement. Indeed, the wake consists of in-phase oscillations of the Kármán rollers; this leads to the formation of aligned lambda-shaped vortices similar to those studied by Meiburg & Lasheras (1988). Their spanwise wavelength is of the order of the size of the computational box, and they are associated with the growth of the $m_{2,1}$ spectral mode. Notice that, in this case of natural transition of the wake (still without rotation), one does not obtain the helical-pairing topology which was

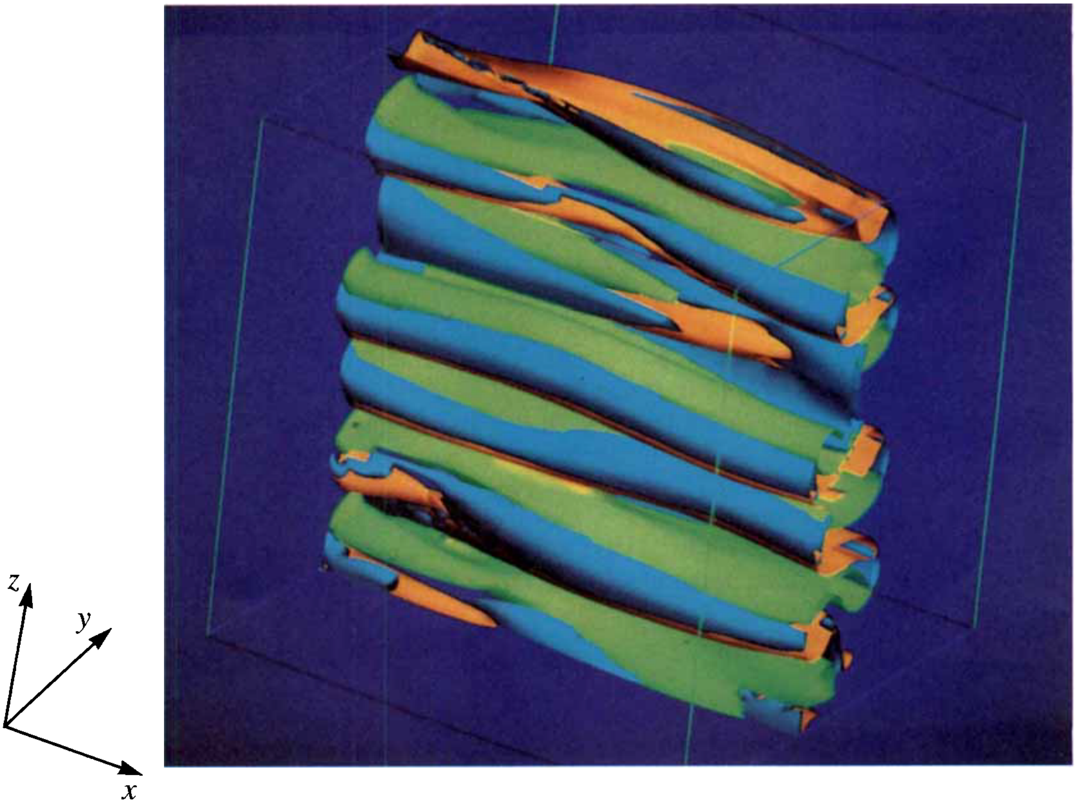

FIGURE 15. Anticyclonic mixing layer at $R_o^{(i)} = -5$, natural transition. Relative vorticity isosurfaces at $t = 22.3\,\delta_i/|U_0|$. $\omega_z = 45\%$ of $|\omega_{2D}^{(i)}|$, blue; $\omega_l = 45\%$ of $|\omega_{2D}^{(i)}|$ coloured by the sign of ω_x, orange $\omega_x < 0$, green $\omega_x > 0$.

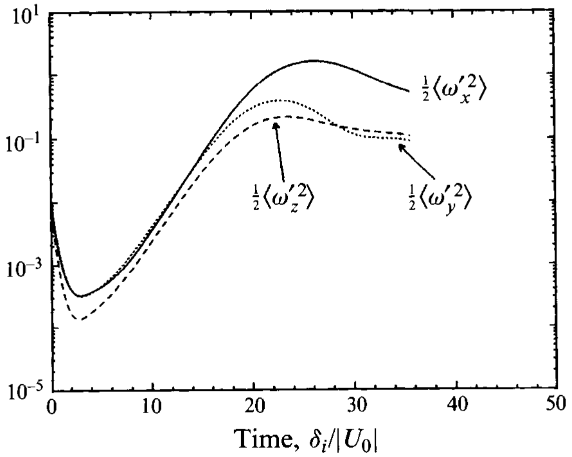

FIGURE 16. Anticyclonic mixing layer at $R_o^{(i)} = -5$, natural transition. Time evolution of the half-variance of the vorticity fluctuation components $\frac{1}{2}\left\langle\omega'^2_x\right\rangle, \frac{1}{2}\left\langle\omega'^2_y\right\rangle$, and $\frac{1}{2}\left\langle\omega'^2_z\right\rangle$ (normalized by $\omega_{2D}^{(i)2}$).

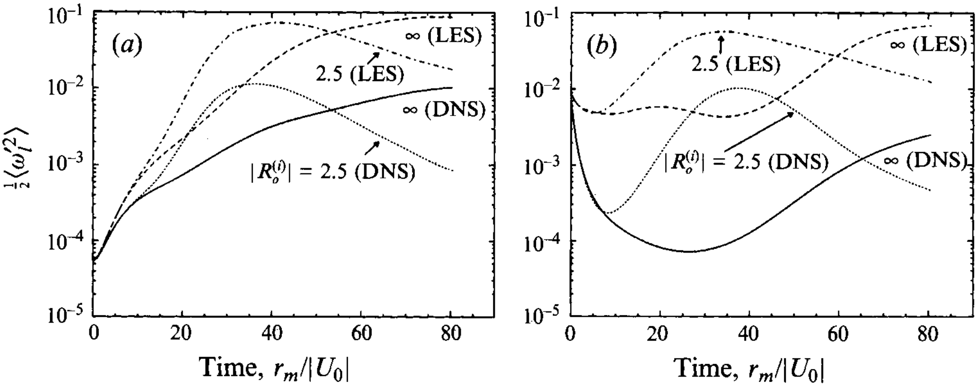

FIGURE 17. Plane wake. Time evolution of the relative longitudinal vorticity half-variance $\frac{1}{2}\langle\omega_l'^2\rangle = \frac{1}{2}\langle\omega_x'^2 + \omega_y'^2\rangle$ (normalized by $\omega_{2D}^{(i)2}$) obtained through direct numerical simulation (DNS) and through large-eddy simulation (LES), for $|R_o^{(i)}| = \infty$, $|R_o^{(i)}| = 2.5$. (*a*) Forced transition; (*b*) natural transition.

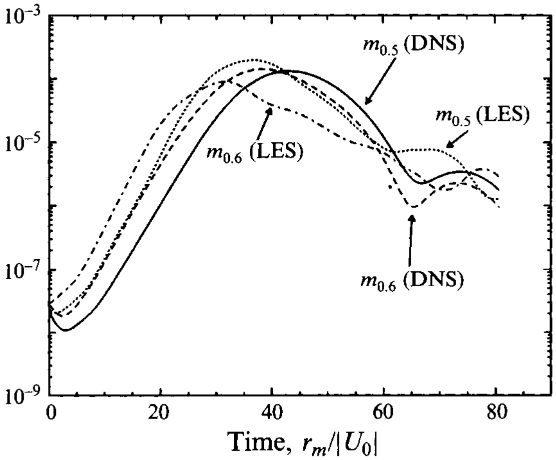

FIGURE 18. Plane wake at $|R_o^{(i)}| = 2.5$, natural transition. Comparison of the time evolution of the kinetic energy in the longitudinal spectral modes $m_{0,5}$ and $m_{0,6}$ as given by the DNS and by the LES.

obtained for the mixing layer by Comte *et al.* (1992). This type of dislocated structure of the far wake had been obtained experimentally by Cimbala, Nagib & Roshko (1988) at low Reynolds number. It has been shown by Williamson & Prasad (1993), however, that it is due to a resonance between two-dimensional waves generated by the instability of this far wake, and oblique Kármán vortices shed in the near wake.

In the rotating case, the contribution of the Coriolis term to the pressure is discarded here, and the scalar considered could be qualified as the 'ageostrophic' pressure. As opposed to the vorticity iso-surfaces, which are very irregular because of the influence of small-scale structures, the low-pressure contours are very smooth. In the forced transition case, they clearly display the longitudinal hairpin vortices of the anticyclonic side of the wake, superposed with the cyclonic Kármán rolls (see figure 20*a*). Their spanwise wavelength is approximately one-fourth of the computational domain width, as in the direct numerical simulation presented on figure 12(*c*). Longitudinal low-pressure structures are also distinguishable during the

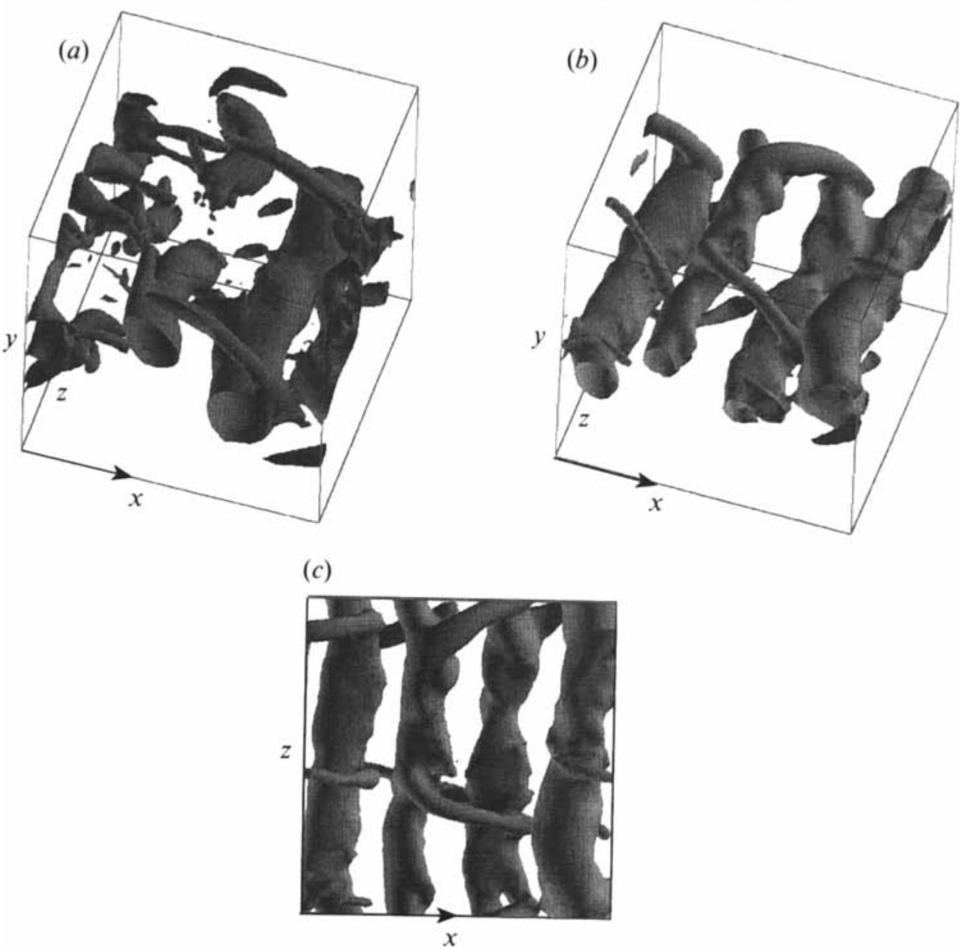

FIGURE 19. Plane wake ($|R_o^{(i)}| = \infty$), at $t = 65.5\ r_m/|U_0|$. (*a*) Forced transition. The gray surfaces delimit the regions where the pressure $\overline{P}$ defined by (4.7) satisfies $\overline{P}_{min} \leqslant \overline{P} \leqslant 0.29\overline{P}_{min}$. $\overline{P}_{min}$ is the instantaneous pressure minimum ($\overline{P}_{min} < 0$). (*b,c*) Natural transition case, two different views of the same iso-surfaces. The iso-contour values are the same as in (*a*).

natural transition of the wake, although the small-scale activity is so important that it even appears on the low-pressure contours (see figure 20*b*).

4.4. *Vorticity stretching mechanisms*

We here focus on the direct numerical simulation of the mixing layer at $R_o^{(i)} = -5$. A crucial question to be answered concerns the origin of the hairpin vortices observed both in the forced and natural transition cases. For that, we examine the instantaneous *absolute* vortex lines where the longitudinal vorticity component ω_x exceeds a certain threshold. Figure 21 displays, in the forced transition case at $t = 26.8\delta_i/|U_0|$, the instantaneous *absolute* vortex lines (figure 21*a*) and the corresponding iso-surfaces of high *relative* vorticity modulus (figure 21*b*). They are very well correlated, which shows that the relative vorticity concentrations are in fact composed of absolute vortex lines concentrations. In the legs of the vortices, the absolute vortex lines are perfectly longitudinal. Therefore, these regions correspond to nearly zero absolute spanwise vorticity (i.e. the local Rossby number is approximately -1). Notice also

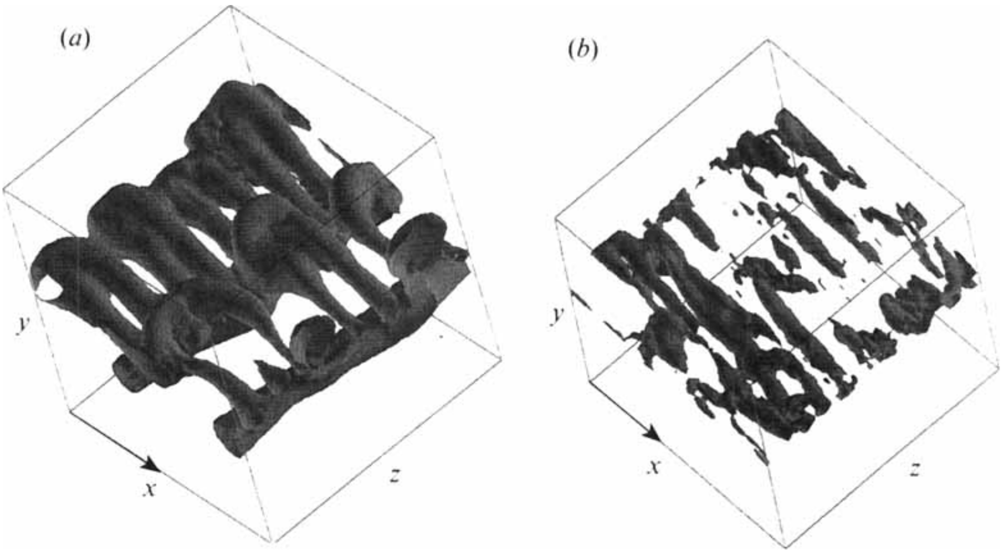

FIGURE 20. Plane wake at $|R_o^{(i)}| = 2.5$ and at $t = 32.3\ r_m/|U_0|$. (*a*) Forced transition. Here, the gray surfaces delimit the regions where the 'ageostrophic' pressure $\overline{P}_{ag}$ satisfies $\overline{P}_{ag}^{min} \leqslant \overline{P}_{ag} \leqslant 0.29\overline{P}_{ag}^{min}$. $\overline{P}_{ag}^{min}$ is the instantaneous pressure minimum ($\overline{P}_{ag}^{min} < 0$). (*b*) Natural transition. Same as (*a*) but for $\overline{P}_{ag}^{min} \leqslant \overline{P}_{ag} \leqslant 0.48\overline{P}_{ag}^{min}$.

that these vortices, which have a zero spanwise absolute vorticity and are longitudinal, are not parallel to the relative vorticity; the latter has a longitudinal component equal to the longitudinal absolute vorticity, and a spanwise component of -2Ω.

Let us now turn to the case of natural transition. As previously shown in figure 14, the fastest growing mode $m_{0,6}$ predicted by the linear-stability analysis remains the most energetic during a long period (until $t < 30\ \delta_i/|U_0|$). This quickly yields purely longitudinal vortices as exhibited in figure 15. These vortices have a spanwise wavelength λ_s corresponding to the fastest mode. The examination of the time evolution of the absolute vortex lines shows that the flow undergoes very distinct stages. In the first stage, the vorticity dynamics are dominated by quasi-linear mechanisms. All the absolute vortex lines oscillate in phase in the streamwise direction with a spanwise wave-length λ_s, which corresponds to the longitudinal mode predicted from linear-stability theory. Both vorticity components ω_x and ω_y undergo similar growth, and the absolute vortex filaments rise approximately at 45° with respect to the x-direction, as shown in figure 22(*a*). In this stage, the vortex dynamics seems to be correctly described by (1.7) and (1.8). In a second stage, a nonlinear stretching occurs and the legs of these vortices become purely longitudinal. The latter correspond again to regions of near zero absolute spanwise vorticity (the local Rossby number is approximately -1). Figure 22(*b*) shows that in the final stage, the flow has undergone a complete change in the vortex topology as compared to figure 22(*a*): the hairpin vortices rise weakly with respect to the horizontal plane (to about 20°). Furthermore, the absolute vortex lines are highly concentrated within the legs, and the resulting absolute vortex tubes are extremely elongated. As previously emphasized, ω'_x dominates ω'_y; by the end of the computation $\omega'_x \approx 1.4\ \omega_{2D}^{(i)}$ and $\omega'_y \approx 0.9\ \omega_{2D}^{(i)}$.

Our aim here is to test the phenomenological theory proposed by Lesieur *et al.*

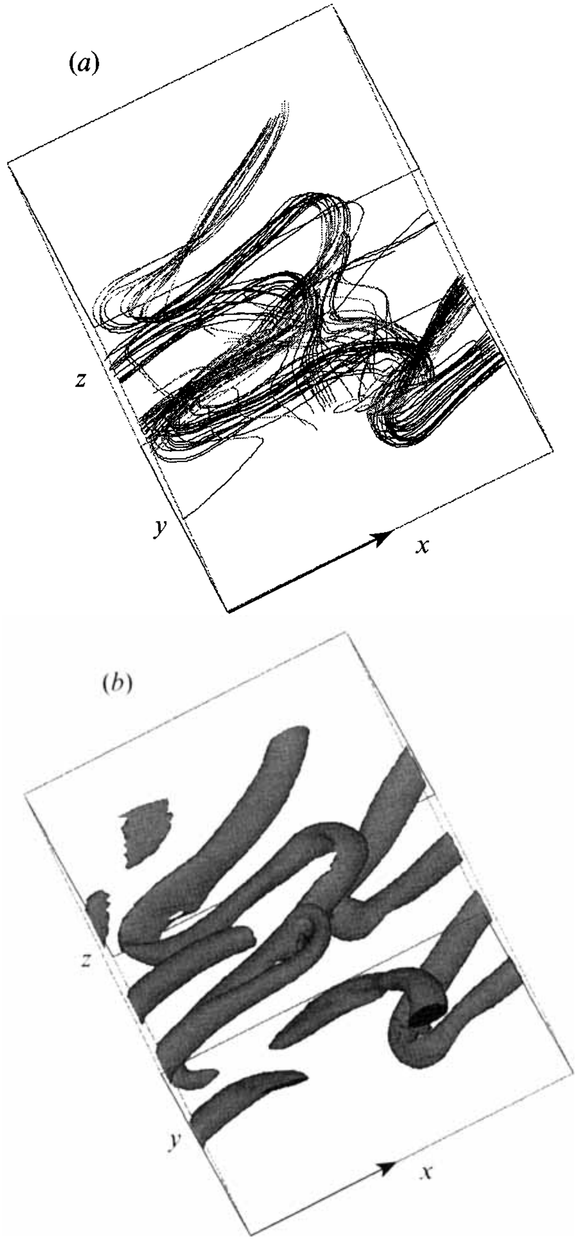

FIGURE 21. Anticyclonic mixing layer at $R_o^{(i)} = -5$, forced transition. Same calculation as figure 8(*c*): (*a*) absolute vortex lines, (*b*) isosurface of the relative vorticity modulus $||\vec{\omega}|| = (\omega_x^2 + \omega_y^2 + \omega_z^2)^{1/2}$ corresponding to $||\vec{\omega}|| = 78\%$ of $|\omega_{2D}^{(i)}|$.

(1991) and identify the regions of the flow in which the maximum vorticity stretching takes place. Since we focus here on the local dynamics, it is useful to define a Rossby number local in space and time such as:

$$R_o^l(\boldsymbol{x}, t) = \frac{\omega_z(\boldsymbol{x}, t)}{2\Omega} \; . \tag{4.8}$$

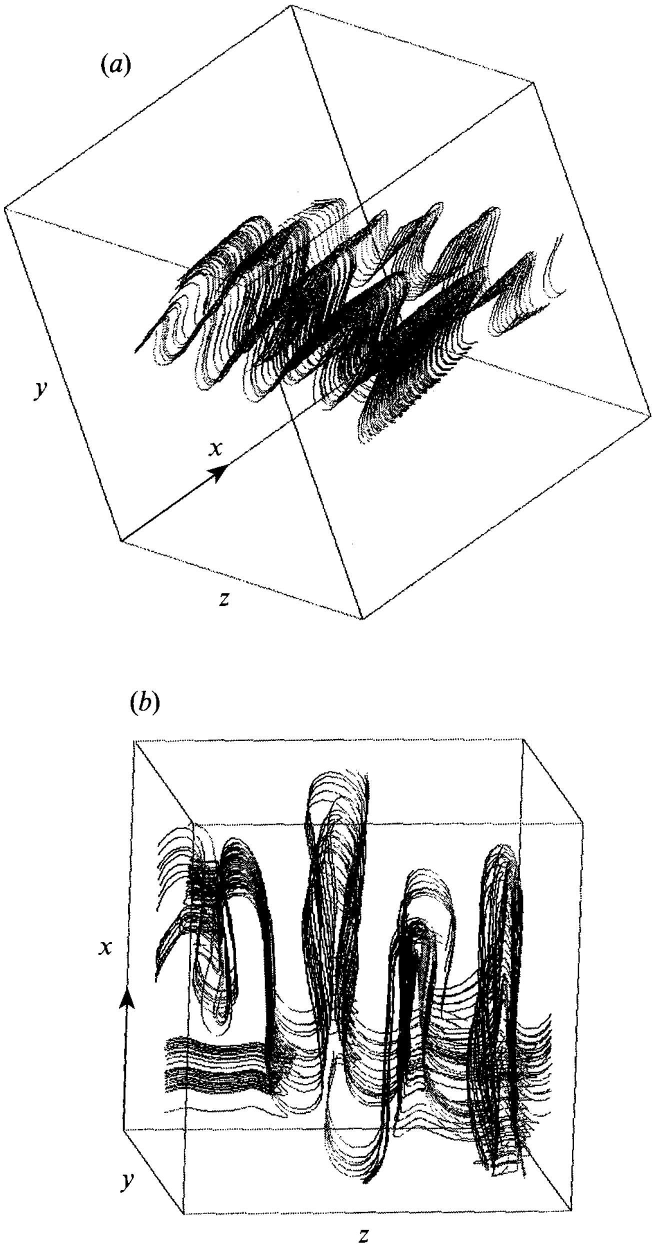

FIGURE 22. Anticyclonic mixing layer at $R_o^{(i)} = -5$, natural transition. Same calculation as figure 15: absolute vortex filaments at (*a*) $t = 17.8\,\delta_i/|U_0|$, (*b*) $t = 22.3\,\delta_i/|U_0|$. The contrast change corresponds to a change of sign of ω_x.

Note that it can be written as

$$R_o^l(\boldsymbol{x},t) = \frac{1}{2\Omega}\left(-\frac{\mathrm{d}\bar{u}(y,t)}{\mathrm{d}y}\right) + \frac{\omega_z'(\boldsymbol{x},t)}{2\Omega} = R_o(y,t) + R_o'(\boldsymbol{x},t). \tag{4.9}$$

Except for the time dependency, $R_o(y,t)$ is the local Rossby number originally introduced by Pedley(1969) (see § 1.1). $R_o'(\boldsymbol{x},t)$ is associated with the fluctuating field.

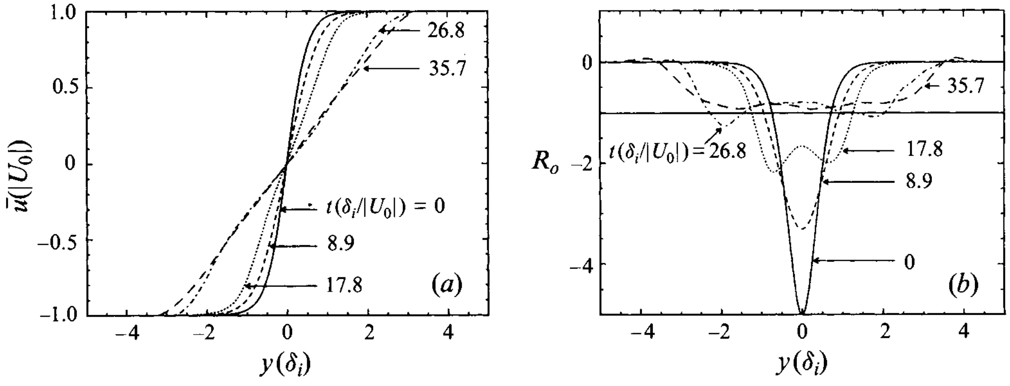

FIGURE 23. Anticyclonic mixing layer at $R_o^{(i)} = -5$, natural transition. (*a*) Time evolution of the mean velocity profile $\bar{u}(y,t)$, normalized by $|U_0|$. y is non-dimensionalized by δ_i and the time unit is $\delta_i/|U_0|$. (*b*) Time evolution of the profile $R_o(y,t)$ (see (4.9)).

Let us first consider how the basic field evolves in the presence of the anticyclonic rotation. Figure 23(*a*) shows the time evolution of the mean velocity profile $\bar{u}(y,t)$. Starting from the initial hyperbolic tangent inflexional shape, the mean profile exhibits, in the highly nonlinear state ($t > 20\ \delta_i/|U_0|$), a long range of nearly constant shear, whose intensity $\mathrm{d}\bar{u}(y)/\mathrm{d}y$ is independent of time. This is confirmed by the profiles $R_o(y,t)$ (see (4.9)) which display by the end of the run ($t = 26.8$ and $35.7\ \delta_i/|U_0|$) a very well defined plateau around the value of -1 (see figure 23*b*). Thus, the mean velocity profile becomes such that its vorticity exactly compensates the solid-body rotation vorticity. Sizeable regions of nearly zero mean absolute vorticity were first observed in the channel flow experiments by Johnston *et al.* (1972), and the recent simulations by Kristoffersen & Andersson (1993) have reproduced this behaviour. These correspond to regions of neutral stability from a linear point of view, and one may be inclined to think that the flow has reached a marginal stability state in which all instability mechanisms would eventually disappear. In the present numerical simulations, we have checked, however, that, during the time period of appearance of the constant-slope range for the mean velocity profile ($t > 20\ \delta_i/|U_0|$), the averaged stretching rate for the dominant vorticity component ω_x

$$\left\langle \omega_x^2 \frac{\partial u}{\partial x} \right\rangle \Big/ \left\langle \omega_x^2 \right\rangle$$

keeps a constant value. This indicates that, by the end of our computation, nonlinear effects still dominate the flow dynamics. Therefore, the present flow configuration seems to provide the conditions in which the weak absolute vorticity stretching mechanism proposed by Lesieur *et al.* (1981) can operate.

We now determine the regions of the flow in which the maximum longitudinal vorticity production is achieved. We focus on ω_x, which is the dominant vorticity component. From (1.2), one can derive the following equation:

$$\omega_x \frac{\mathrm{d}\omega_x}{\mathrm{d}t} = ST(\boldsymbol{x},t) + \nu\omega_x \nabla^2 \omega_x , \tag{4.10}$$

where $ST(\boldsymbol{x},t)$ is the product of ω_x and the ω_x stretching and turning terms:

$$ST(\boldsymbol{x},t) = \omega_x^2 \frac{\partial u}{\partial x} + \omega_x \omega_y \frac{\partial u}{\partial y} + \omega_x 2\Omega \left(R_o^l + 1 \right) \frac{\partial u}{\partial z} \quad , \tag{4.11}$$

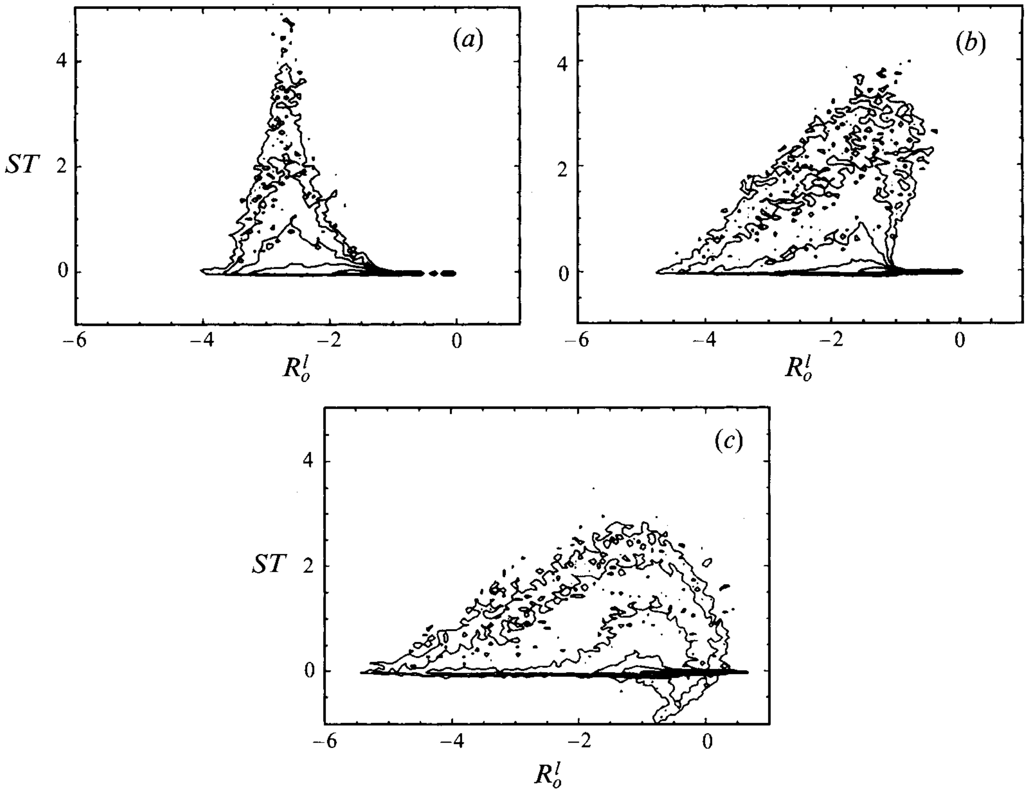

FIGURE 24. Anticyclonic mixing layer at $R_o^{(i)} = -5$, natural transition. Two-dimensional joint probability density function for ST (see (4.11)) versus the local Rossby number R_o^l (see (4.8)). (*a*) $t = 13.4\,\delta_i/|U_0|$; (*b*) $t = 17.8\,\delta_i/|U_0|$; (*c*) $t = 22.3\,\delta_i/|U_0|$. The density contours are logarithmic and spaced by a factor $\sqrt{10}$.

where R_o^l is given by eq. (4.8). We recall that $\omega = (\omega_x, \omega_y, \omega_z)$ is the relative vorticity. We here concentrate on the statistics of ST. Figure 24 shows the two-dimensional joint probability density function for ST versus R_o^l. ST is normalized by its variance $ST_{var} = \langle ST^2 \rangle^{1/2}$. Figure 24(*a*) corresponds to the quasi-linear initial stage ($t = 13.4\ \delta_i/|U_0|$). Although the statistics are noisy because they are deduced from only one flow realization, one can observe that maximum longitudinal vorticity production occurs in the flow regions such that the local Rossby number $R_o^l(x)$ is about -2.8. This is not far from the value of -2.5 predicted by the linear-stability analysis of Yanase *et al.* (1993) and comparable to the quasi-linear theory presented in § 1.2.1. As time proceeds (figures 24*b* and 24*c*), the highest values of the production move progressively towards higher local Rossby numbers, and are concentrated around a value of the order of -1 by late time. Therefore, at this stage, the maxima of longitudinal-vorticity generation are situated in flow regions of weak spanwise absolute vorticity in agreement with the phenomenological theory proposed by Lesieur *et al.* (1991).

5. Conclusions

The present numerical simulations of planar mixing-layers and plane wakes confirm the two-dimensionalization effect of cyclonic rotation and rapid-anticyclonic rotation.

The two-dimensionalization consists in an inhibition of the three-dimensional motions: the stretching mechanisms leading to longitudinal vorticity amplification are prevented, and the energy exchanges are directed preferentially from the mean flow to the two-dimensional component of the motion. The flow two-dimensionalization is confirmed by the spectral kinetic energy distribution, which is mainly concentrated around wavenumber $k_z = 0$; this is in agreement with the predictions of the Taylor–Proudman theorem. In the low Rossby number regime, cyclonic and anticyclonic vortices are respectively low- and high-pressure regions, in agreement with a geostrophic balance.

Both direct and large-eddy simulations show that moderate anticyclonic rotation (for $|R_o^{(i)}| > 1$) greatly enhances longitudinal vorticity stretching. In the present paper, special care is given to the study of the three-dimensional coherent vortex dynamics corresponding to maximum destabilization of the anticyclonically rotating mixing layer and of the anticyclonic side of the wake. Maximum destabilization is achieved for a critical Rossby number, whose value closely corresponds to the predictions of the linear-stability analysis performed by Yanase *et al.* (1993), i.e. $|R_o^{(i)}| \approx 2.5$. In the linear study, the instability appeared on the k_z axis and corresponds to purely longitudinal amplified modes; this instability is referred to as the shear/Coriolis instability. During the early evolution, the most amplified modes found in the computation are in close agreement with the linear-stability predictions. The flow quickly reaches a highly nonlinear state, however, with a wide range of excited modes. The energy of the three-dimensional motion is directly extracted from the mean flow.

We have investigated the influence of the initial perturbation on the growth of longitudinal vortices of the anticyclonically rotating mixing layer and of the anticyclonic side of the wake. First, the case of forced transition is considered, using quasi-two-dimensional noise corresponding to energy preferentially injected into the Kelvin–Helmholtz (or Kármán) mode. Secondly, the natural transition is studied by choosing an initial, three-dimensional white-noise perturbation. In the forced transition case, we observe the simultaneous formation of Kelvin–Helmholtz (or Kármán) vortices and longitudinal hairpin vortices which are stretched in between. The latter originate from the early linear amplification of the shear/Coriolis instability modes. As time goes on, the nonlinear stretching mechanisms produce an important increase of the longitudinal vorticity component. The stretching is particularly intense for the x-component of the vorticity, which quickly dominates the other two components. This ultimately leads to the complete dislocation of the primary rolls and a flow entirely composed of hairpin-shaped longitudinal vortices. The striking feature of these vortices is that they are in fact composed of purely longitudinal *absolute* vortex lines concentrations and correspond to *absolute* vorticity stretching.

In the case of natural transition, we observe the rapid formation of purely longitudinal structures corresponding to regions of high *relative* vorticity. These structures have a spanwise wavelength λ_s corresponding to the fastest shear/Coriolis mode predicted by the linear-stability analysis of Yanase *et al.* (1993). Close examination of the time evolution of the *absolute* vortex lines shows that the flow undergoes very distinct stages. In the first stage, the vorticity dynamics are dominated by quasi-linear mechanisms yielding absolute vortex lines inclined at 45° with respect to the horizontal plane. These are in phase in the longitudinal direction. We have checked that maximum longitudinal vorticity stretching is achieved in the flow regions with a local Rossby number of approximately -2.8. In a second stage, nonlinear stretching mechanisms yield quasi-horizontal longitudinal hairpins of absolute vorticity. As in the forced transition case, these absolute vortex tubes correspond to local Rossby number

≈ -1. The ω_x stretching terms become larger than for ω_y, and those terms are found to be maximum within the legs of the vortices. The dynamics are then dominated by a strong quasi-horizontal stretching of longitudinal *absolute* spanwise vorticity. During that stage, we observe that the background velocity profile exhibits a long range of nearly constant shear whose vorticity exactly compensates the solid-body rotation vorticity.

Both in the forced and natural transition cases, the eventual states are in agreement with the phenomenological theory proposed by Lesieur *et al.* (1991). The longitudinal stretching is initially much more efficient than in the case without rotation. At late times, however, and in the case of the wake, the longitudinal vorticity thus produced undergoes a strong damping. This is certainly due to nonlinear effects which produce an intense cascade towards dissipative scales.

Thus a very efficient mechanism to create intense longitudinal vortices in rotating anticyclonic shear layers is provided, thanks to a linear longitudinal instability followed by a vigorous stretching of absolute vorticity. It would be interesting to look for the existence of these longitudinal vortices in laboratory experiments studying rotating mixing layers and wakes. The same phenomenology should also hold for other types of shear flows submitted to solid-body rotation, such as separated flows, boundary layers and channels, or homogeneous turbulence in a constant shear.

The authors are grateful to D. J. Tritton for many enlightening discussions. C.F. was supported by CONACYT (Mexican Council for Science and Technology), S.Y. by CNRS (Poste Rouge TOAE and INSU) and by INPG, and J.J.R. by UJF (Chaire de Mathématiques Industrielle). Partial support for J.J.R. was provided by the US Office of Naval Research (Contract No. N00014-90-1112). Some of the computations were carried out at the IDRIS (Institut du Développement et des Ressources en Informatique Scientifique, Paris). This work was supported by the CNRS (GDR "Mécanique Fondamentale des Fluides Géophysiques et Astrophysiques").

REFERENCES

Bartello, P., Métais, O. & Lesieur, M. 1994 Coherent structures in rotating three-dimensional turbulence. *J. Fluid Mech.* **273**, 1–29.

Bidokhti, A. A. & Tritton, D. J. 1992 The structure of a turbulent free shear layer in a rotating fluid. *J. Fluid Mech.* **241**, 469–502.

Bradshaw, P. 1969 The analogy between streamline curvature and buoyancy in turbulent shear flow. *J. Fluid Mech.* **36**, 177–191.

Cain, A. B., Ferziger, J. H. & Reynolds, W. C. 1984 Discrete orthogonal function expansions for non-uniform grids using the fast Fourier transform. *J. Comput. Phys.* **56**, 272–286.

Chabert d'Hières, G., Davies, P. A. & Didelle, H. 1988 Laboratory studies of pseudo-periodic forcing due to vortex shedding from an isolated solid obstacle in an homogeneous rotating fluid. In *20th Intl Liège Colloquium on Ocean Dynamics*. Elsevier.

Cimbala, J. M., Nagib, H. M. & Roshko, A. 1988 Large structure in the far wakes of two-dimensional bluff bodies. *J. Fluid Mech.* **190**, 265–298.

Comte, P., Lesieur, M. & Lamballais, E. 1992 Large- and small-scale stirring of vorticity and a passive scalar in a 3-D temporal mixing layer. *Phys. Fluids* A **4**, 2761–2778.

Etling, D. 1990 Mesoscale vortex shedding from large islands: a comparison to laboratory experiments in rotating stratified flows. *Met. Atmos. Phys.* **43**, 145.

Flores, C. 1993 Etude numérique de l'influence d'une rotation sur les écoulements cisaillés libres. PhD dissertation, National Polytechnic Institute, Grenoble.

Guo, Y. & Finlay, W. H. 1991 Splitting, merging and wavelength selection of vortices in curved and/or rotating channel flow due to Eckhaus instability. *J. Fluid Mech.* **228**, 661–691.

HART, J. E. 1971 Instability and secondary motion in a rotating channel flow. *J. Fluid Mech.* **45**, 341–351.

JOHNSTON, J. P., HALLEEN, R. M., & LEZIUS, D. K. 1972 Effects of spanwise rotation on the structure of two-dimensional fully developped turbulent channel flow. *J. Fluid Mech.* **56**, 533–557.

KIM, J. 1983 The effect of rotation on turbulence structure. In *Proc. 4th Symp. on Turbulent Shear Flows, Karlsruhe*, pp. 6.14–6.19.

KRISTOFFERSEN, R. & ANDERSSON, H. I. 1993 Direct simulations of low-Reynolds-number turbulent flow in a rotating channel. *J. Fluid Mech.* **256**, 163–197.

LESIEUR, M., YANASE, S. & MÉTAIS, O. 1991 Stabilizing and destabilizing effects of a solid-body rotation upon quasi-two-dimensional shear layers. *Phys. Fluids* A **3**, 403–407.

MEIBURG, E. & LASHERAS, J. C. 1988 Experimental and numerical investigation of the three-dimensional transition in plane wakes. *J. Fluid Mech.* **190**, 1–37.

MÉTAIS, O. & LESIEUR, M. 1992 Spectral large-eddy simulation of isotropic and stably-stratified turbulence. *J. Fluid Mech.* **239**, 157–194.

MÉTAIS, O., RILEY, J. J. & LESIEUR, M. 1993 Numerical simulations of stably-stratified turbulence. *Ninth Symp. on Turbulent Shear Flows, Kyoto, Japan, August 16-18*, pp. 1-3-1,1-3-6.

MÉTAIS, O., YANASE, S., FLORES, C., BARTELLO, P. & LESIEUR, M. 1992 Reorganization of coherent vortices in shear layers under the action of solid-body rotation. In *Turbulent Shear Flows VIII*, pp. 415–430. Springer.

MICHALKE, A. 1964 On the inviscid instability of the hyperbolic-tangent profile. *J. Fluid Mech.* **19**, 543–556.

PEDLEY, T. J. 1969 On the stability of viscous flow in a rapidly rotating pipe. *J. Fluid Mech.*, **35**, 97–115.

POTTER, M. C. & CHAWLA, M. D. 1971 Stability of boundary layer flow subject to rotation. *Phys. Fluids* **14**, 2278–2281.

ROTHE, P. H. & JOHNSTON, J. P. 1979 Free shear layer behaviour in rotating systems. *Trans. ASME: J. Fluids Engng* **101**, 117–119.

SATO, H. & KURIKI, K. 1961 The mechanism of transition in the wake of a thin plate placed parallel to a uniform flow. *J. Fluid Mech.* **11**, 321–352.

TAFTI, D. K. & VANKA, S. P. 1991 A numerical study of the effects of spanwise rotation on turbulent channel flow. *Phys. Fluids* A **3**, 642–656.

TRITTON, D. J. & DAVIES, P. A. 1985 Instabilities in geophysical fluid dynamics. In *Hydrodynamic Instabilities and the Transition to Turbulence* (ed. H. L. Swinney & J. P. Gollub), pp. 229–270. Springer.

WATMUFF, J. H., WITT, H. T. & JOUBERT, P. N. 1985 Developing turbulent boundary layers with system rotation. *J. Fluid Mech.* **157**, 405–448.

WILLIAMSON, C. & PRASAD, A. 1993 Acoustic forcing of oblique wave resonance in the far wake. *J. Fluid Mech.* **256**, 315–341.

WITT, H. T. & JOUBERT, P. N. 1985 Effect of rotation on a turbulent wake. In *Proc. 5th Symp. on Turbulent Shear Flows, Cornell*, pp. 21.25–21.30.

YANASE, S., FLORES, C., MÉTAIS, O. & RILEY, J. J. 1993 Rotating free shear flows Part 1: Linear stability analysis. *Phys. Fluids* A **5**, 2725–2737.